PHYSICAL REVIEW B **74**, 174121 (2006)

Raman spectra of the ferroelectric phase of SrTi^{18}O$_3$: Symmetry and domains below T_c and the origin of the phase transition

Takeshi Shigenari,[1] Kohji Abe,[1] Tomohiko Takemoto,[1] Osamu Sanaka,[1] Takashi Akaike,[1] Yoshihide Sakai,[1] Ruiping Wang,[2] and Mitsuru Itoh[3]
[1]*Department of Applied Physics and Chemistry, University of Electro-Communications, Chofu-shi, Tokyo 182-8585, Japan*
[2]*National Institute for Advanced Industrial Science and Technology, Tsukuba 305-8568, Japan*
[3]*Materials and Structures Laboratory, Tokyo Institute of Technology, 4297, Nagatsuda, Midori, Yokohama, 226-8603, Japan*

(Received 1 May 2006; revised manuscript received 28 August 2006; published 30 November 2006)

Polarized Raman spectra of isotope substituted SrTi^{18}O$_3$ (STO18) crystals were studied in the ferroelectric phase below T_c=24.5 K. Samples were confirmed to be a single domain in the tetragonal phase ($T_c < T < T_0$ =108 K). Raman spectra in various phonon propagation directions $\vec{K}_p$ were found to satisfy the selection rules for orthorhombic C_{2v} symmetry with the spontaneous polarization $\vec{P}$ parallel to the tetragonal axes, either $[110]_c$ or $[1\bar{1}0]_c$. Below T_c, STO18 is inhomogeneous and consists of a number of small ferroelectric domains as well as remnants of the tetragonal structure. Soft TO modes originated from the lowest Γ_{15} mode in cubic phase were observed at 20 and 12.5 cm^{-1}. On heating, these modes soften but do not freeze at T_c. Near T_c, a quasielastic scattering component appears and its intensity critically increases. Although for temperatures far from T_c, the transition is promoted by the softening of the TO modes, the appearance of $\vec{P}$ at T_c cannot be attributed to the freezing of Slater mode since $\vec{P}$ is *not* parallel to the cubic axis $[100]_c$. Origin of the relaxational mode near T_c and the direction of $\vec{P}$ are discussed in terms of the orientational ordering of locally polarized clusters which already exist above T_c. These results indicate that the phase transition in STO18 is a peculiar transition and has both order-disorder and displacive nature.

DOI: 10.1103/PhysRevB.74.174121 PACS number(s): 77.84.Dy, 77.80.Bh, 77.80.Dj, 78.30.−j

I. INTRODUCTION

A pure SrTiO$_3$ crystal is often called as a quantum paraelectric.[1] In spite of the remarkable increase in the dielectric constant and the softening of a polar phonon mode, it does not undergo a ferroelectric phase transition down to 0 K. Low temperature dielectric constant increases to about 30 000 at about 30 K on cooling and then it remains temperature independent. It was known that the application of stress perpendicular to *c*-axis in the tetragonal phase of SrTi^{16}O$_3$ (STO16) (Ref. 2) and also the doping of Ca-ion to STO16 (Ref. 3) induces ferroelectricity at low temperatures. However, intrinsic ferroelectric transition has not been known in STO. Recently Itoh *et al.*[4] found that a ferroelectric phase transition takes place at about T_c=24 K by substituting ^{18}O for ^{16}O in STO. Thus a STO18 crystal undergoes successive phase transitions from cubic (O_h^1, $Pm\bar{3}m$) to tetragonal (D_{4h}^{18}, $I4/mcm$) and to a lower (unknown) symmetry structure at T_c=24 K.[5] The transition temperature to D_{4h}^{18} is about T_0=108 K which is slightly higher than that of STO16 (T_0=105 K). As with STO16, the crystal axes of STO18 in the tetragonal phase are rotated by 45° around one of the cubic axis $[001]_c$.

The ferroelectricity by the isotope substitution was an unexpected phenomenon and a number of studies have been done since its discovery. The mechanism of the transition, however, has not been clarified yet. Even the symmetry of the ferroelectric phase and the direction of the spontaneous polarization have not been known. As for the phonon behavior in STO16, the existence of a strongly polarized mode, which is one of Γ_{15} modes in the cubic phase, has been well known since 1950's. The mode is often called Slater mode[6] or ferroelectric TO mode. Softening in a wide temperature range of STO16 was first observed by IR spectroscopy.[7] Its frequency ~90 cm^{-1} at room temperature decreases down to ~15 cm^{-1} at about 30 K but it rounds off on further cooling as revealed by neutron scattering[8] and hyper-Raman scattering.[9–11]

For STO18, until now, optical and spectroscopic measurements, e.g., birefringence,[12] Raman,[13–15] Brillouin scattering,[16] SHG,[17,18] and hyper-Raman scattering[19] have been reported. In these measurements, various qualitative differences between the two phases were observed and they clearly indicate the lowering of the macroscopic symmetry below T_c. However, the strange thing is that in contrast to these optical and spectroscopic measurements, structural variations by this transition were found to be very small. The specific heat measurement showed no anomaly at T_c (Ref. 20) and the variation in lattice parameters are too small to be detected by the conventional diffraction methods. Only a small variation in the ratio a/c was detected by synchrotron-orbital-radiation (SOR) topography.[21] Recent report on neutron diffraction[22] showed that above T_c, the TO(E_u) mode softens almost in the same way as that observed in STO16.[8] Only difference between STO18 and STO16 is the increase of the quasielastic scattering intensity around T_c but its origin has not been known.

Until now no definite mode assignment has been successfully done. The assignment of phonons in STO18 is not easy because of the appearance of the tetragonal domains below T_0, particularly in the neutron scattering which requires a large sample. Since a soft mode is always Raman active below T_c for any displacive structural phase transitions, Raman scattering is a powerful method to detect the soft mode.

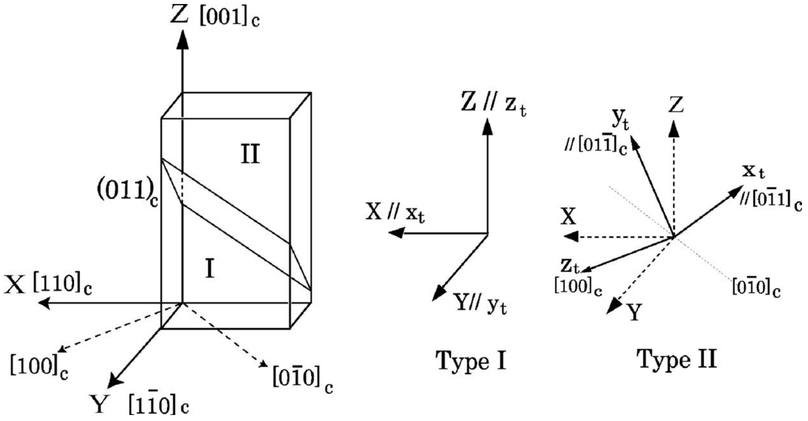

FIG. 1. Sample shape and the two possible domain types in the tetragonal phase. Subscripts c and t denote cubic and tetragonal phase, respectively. Capital letters X,Y,Z represent the directions of sample edges and also the tetragonal axes in a type I domain.

In this respect, it is important to investigate the low frequency phonon spectra by Raman scattering and to see how this transition is related to the Γ_{15} (Slater) mode and also to the R_{25} mode which is the soft mode responsible to the structural phase transition at T_0. If the lattice instability were the origin of this transition, softening and freezing of the ferroelectric TO mode would take place on approaching T_c.

Recently, Blinc's group has shown by NMR that there exist polarized rhombohedral clusters in perovskite crystals such as $BaTiO_3$ and $SrTiO_3$.[23] The custers have polarization along the $[111]_c$ directions. Because of the local symmetry breaking in these clusters, the ferroelectric mode becomes Raman active. Taniguchi *et al.*[24] measured Raman spectra of partially ^{18}O substituted STO18 (less than the critical concentration $x_c=33\%$) and showed the softening of E_u mode down to about 7 cm^{-1} and slight hardening below 10 K, and it was suggested that the softening of Slater-type polar mode before the onset of the ferroelectric transition. However, without the knowledge of the relation with polar direction of the locally polarized region, any assignment would not be conclusive.

Raman spectra below T_c from a highly substituted STO18, give a more detailed information about phonons in STO18. In our previous studies,[14,15] below T_c, two modes which partially soften on heating were observed and they are very similar to those observed in Ca-doped STO16 below T_c.[25] This sugests that the two temperatore dependent modes are related to the ferroelectric TO(E_u) modes in the tetragonal phade. In these spectra, however, correct mode assignments were difficult because of the follwing reasons: (i) lack of the confirmation of the tetragonal domain structure, (ii) no definite information on the symmetry and the direction of $\vec{P}$, and (iii) lack of the proper consideration on TO/LO splitting which depends on the phonon propagation direction $\vec{K}_p$. As for the symmetry below T_c, we proposed orthorbombic[14] symmetry from Raman, while trigonal symmtry was suggested by Kleeman[17] and Uesu[18] from SHG studies.

In this paper, after the description of experimental conditions in Sec. II, we report in Sec. III on the results of the optical measurements to confirm the tetragonal domain structure and to find the principal directions of refractive index below T_c. In Sec. IV, wide range spectra are shown and the appearance of several new peaks below T_c is reported. Section V is the main part of the paper which shows the polarization and temperature dependencies of Raman spectra in various scattering geometries. They are compared with the selection rules expected for orthorhombic symmetry C_{2v} with polar axis along $[110]_c$ and $[1\bar{1}0]_c$. Results on the mode assignments are illustrated in Fig. 9. In Sec. VI, we discuss the temperature behavior of the soft modes and the relaxational mode which appear near T_c. A possible model is given which explains the relation between the relaxational mode and the rhombohedrally polarized local clusters above T_c. Summary and conclusions are given in Sec. VII.

II. EXPERIMENTAL

Single crystals $SrTiO_3$ with different substitution ratios 83% ($T_c\sim 21.5$ K), 96% ($T_c\sim 24.2$ K), 97% ($T_c\sim 24.3$ K), and 99% ($T_c\sim 24.7$ K) were used. Hereafter we denote a sample with $x\%$ substitution as STO18-x.[26] Most Raman data were taken from the last two samples. Except for small differences in T_c, Raman spectra in the high substitution samples were very similar and reproducible for repeated experiments. Considering the overall accuracy of temperature measurements, we use $T_c=24.5$ K both for STO18-97 and STO18-99.

Samples are thin plates of size $0.3\times 2(\text{or } 3)\times 7$ mm^3 with the widest plane $(110)_c$, and the longest and the shortest edges are parallel to $[001]_c$ and $[110]_c$, respectively. In the following, directions of the sample edges are referred to as (X,Y,Z) as shown in Fig. 1. A sample was set on a copper holder without using any glue. He gas flow type cryostat with temperature stability better than 0.1 K was used.

Using crossed polarizers (Nicols) and a white light source, domain structures in tetragonal and ferroelectric phases were visually checked through the $(110)_c$ surface before each Raman measurement. STO18-83 and -96, which were used in the earlier stage,[14] were found to include many different types of tetragonal domains, whereas STO18-97 and -99 are composed of a single type I domain as shown in Fig. 2 and in the next section.

Raman spectra were measured using an Ar$^+$ laser (514.5 nm, 100–200 mW) and a double monochromator (Jobin-Ybon U1000). The incident laser was focused so that the scattering volume is a cylinder of about 100 μm in diameter. The length of the laser path in a sample is from 7–0.3 mm depending on the scattering geometry. Effective

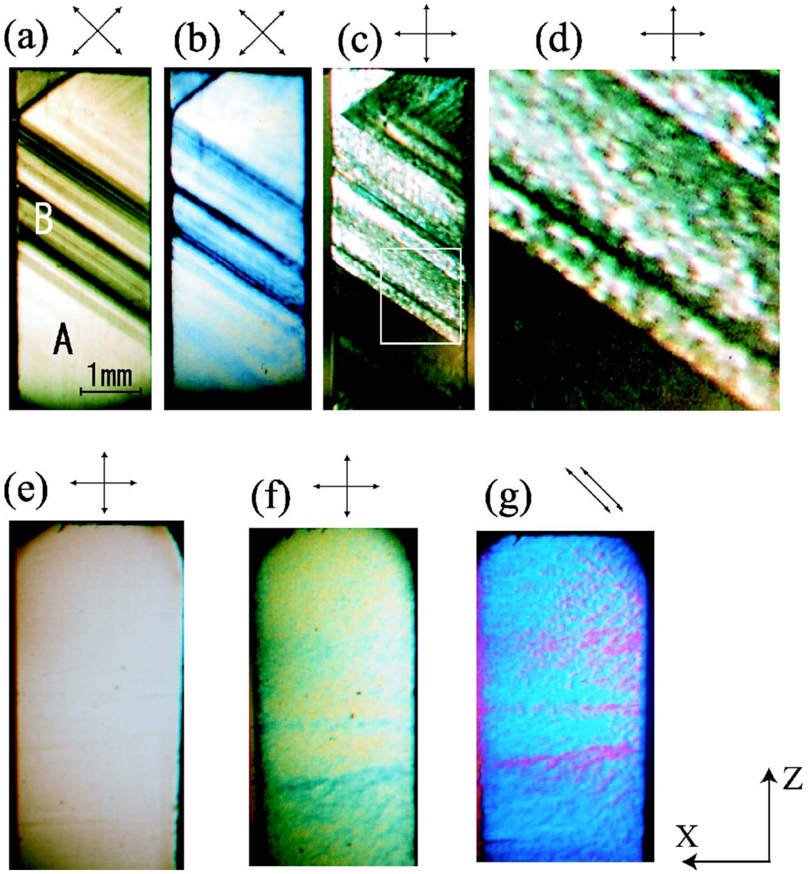

FIG. 2. (Color online) Optical images of domain structures. Directions of crossed Nicols are shown by arrows. (a)–(d) are the images of STO18-96 sample and (e)–(g) are the images of STO18-97 sample. (a) is at 50 K and (b)–(d) are at 10 K. (d) is a magnified image of the white rectangular part in (c). (e) is at 40 K and (f) and (g) are at 10 K. (g) is taken with parallel Nicols and its color is different from (f).

area for scattering was monitored by a periscope inside the monochromator.

Sample temperature was measured by a AuFe-Chromel thermocouple stuck to the sample holder and also by a platinum resistor fixed to the cold head of cryostat. When the laser illumination is on, thermocouple temperature increases by about 2 K at the lowest temperature ($\sim$5 K) and less near T_c. The temperature increase does not mean the increase of sample temperature as we confirmed from the absence of the laser power dependence of the soft mode frequency. The apparent heating is due to the illumination of the transmitted and scattered light on the thermocouple. Overall accuracy of temperature is about ±1 K.

III. OPTICAL OBSERVATIONS AND DOMAINS ABOVE AND BELOW T_c

Since the tetragonal z axis z_t can be one of three cubic $[100]_c$ directions, two types of domain orientations in the tetragonal phase may exist. In a type I domain, the z_t axis is parallel to Z and lies in the sample plane, while in a type II domain it is perpendicular to Z and out of the plane either parallel to $[100]_c$ or $[010]_c$. Type I and type II domains are separated diagonally by $(011)_c$ twin boundaries as illustrated in Fig. 1.

Figures 2(a) and 2(b) are the microscopic images of domain structures in STO18-96 observed at 50 K ($>T_c$) and at 10 K ($<T_c$), respectively. These images are taken with crossed Nicols tilted from Z axis by 45° since the whole area of the sample becomes dark when the crossed Nicols are parallel or perpendicular to Z. Boundaries between the type I and II are clearly observed.

Long and thin sheet type of STO16 samples with $(110)_c$ plane are known to be in favor of the formation of a single (tetragonal) domain.[27] However, we found the whole area of a sample are not always covered by a single domain and domain patterns are sensitive to strains, such as positions of glue (if it were used) to hold the sample. For a free-standing sample, however, domain patterns appear reproducibly after a number of temperature cycles. Presence of the different types of domains in a sample makes the Raman spectra much complicated.

The uniform area A in Fig. 2(a) of sample STO18-96 and the whole area of ST18-97 [Fig. 2(e)] are a tetragonal domain of type I as confirmed by Raman spectra described in the next section. The diagonal lines and stripes in Fig. 2(a) are tilted from Z axis by $\sim$54° as expected for the boundary between type I and II domains. So the dark striped area as B in Fig. 2(a) are considered to be composed of many thin domains with type I and II.

Below T_c, the global pattern [Fig. 2(b)] is similar to that (a) indicating that directions of the principal axes of refractive index in $X-Z$ plane do not change by the transition. This means that $\vec{P}$ appears in a plane perpendicular to z_t in agreement with the birefringence measurement by Yamanaka *et al.*[12] and also with our recent depolarization measurement.[28]

Inside the stripes, granular patterns appear as shown in Figs. 2(c) and 2(d). Size of the grains which we consider as ferroelectric domains are less than 50 μm. The granular pat-

TABLE I. Irreducible representations and their basis for D_{4h}. $X=[110]_c$, $Y=[1\bar{1}0]_c$, and $Z=[001]_c$ are the crystal axes in the tetragonal phase, which coincide with the sample edges of the type-I domain (Fig. 1). Numbers of modes at the Γ point and the symmetries in O_h and C_{2v} are shown in the third and fourth columns. The last two columns show Raman activite polarization configurations in the scattering geometry $X(\ ,\ )\bar{Y}$. V and H stand for the polarization of light being vertical and horizontal to the scattering plane, respectively. The star means the mode is Raman inactive.

		No. of modes at Γ		symmetry	Raman activity in $X(\ ,\ )\bar{Y}$	
D_{4h}	basis	in D_{4h}	from O_h	in C_{2v}	in D_{4h}	in C_{2v}
A_{1g}	X^2+Y^2, Z^2	1	R_{25}	A_1	VV	$VV(=ZZ)$
A_{2g}	$XY(X^2-Y^2)$	2	$R'_2+R'_{12}$	B_2	$\star$	$HH(=XY)$
B_{1g}	X^2-Y^2	1	R'_{12}	A_1	$\star$	VV
B_{2g}	XY	2	$2R_{15}$	B_2	HH	HH
E_g	(YZ,ZX)	3	$R_{25}+2R_{15}$	A_2+B_1	HV, VH	HV, $VH(=YZ,ZX)$
A_{1u}	$XYZ(X^2-Y^2)$	1	R'_{25}	A_2	$\star$	HV,VH
A_{2u}	Z	4	$4\Gamma_{15}$	B_1	$\star$	HV,VH
B_{1u}	$Z(X^2-Y^2)$	0		B_1	$\star$	HV,VH
B_{2u}	ZXY	1	Γ_{25}	A_2	$\star$	HV,VH
E_u	(X,Y)	6	$4\Gamma_{15}+\Gamma_{25}+R'_{25}$	A_1+B_2	$\star$	A_1 in VV, B_2 in HH

terns were hardly observed in the homogeneous area A.

Images from the STO18-97 sample are shown in Fig. 2(e) for 40 K and in Figs. 2(f) and 2(g) for 10 K. No diagonal boundaries are seen and it looks homogeneous above T_c. The relatively coarse and irregular patterns and stripes seen below T_c may be due to the surface roughness caused during the sample preparation process. Main difference by the transition is the appearance of the color below T_c (See color online). Sensitive variation of the color is also seen for different position of Nicols as shown in Figs. 2(f) and 2(g). Such a variation is attributed to a bulk property which indicates that the dispersion of the refractive index $n(\omega)$ significantly increases below T_c.

IV. SYMMETRY OF PHONONS AND RAMAN SPECTRA IN WIDE FREQUENCY RANGE

A. Symmetry of phonons in STO18

First we review the change of symmetry of phonons in STO in cubic O_h^1, tetragonal D_{4h}^{18} and the ferroelectric phases. Since as we see later, it is highly probable that $\vec{P}$ is along the tetragonal axes, the symmetry of the ferroelectric phase is assumed to be orthorhombic C_{2v} with the unique axis parallel to either $X=[110]_c$ or $Y=[1\bar{1}0]_c$. The possibility of rhombohedral (C_{3v}) symmetry with $\vec{P}\|[111]_c$ or the orthorhombic (C_{4v} or C_{2v}) symmetry with $\vec{P}\|[001]_c$ are rejected since the existence of the Z component of $\vec{P}$ contradicts the optical measurements mentioned in the previous section. Moreover, observed Raman spectra (shown in Sec. V) do not satisfy the selection rules for these symmetries.

Fifteen vibrational modes of STO at Γ point in O_h^1 change their symmetry in D_{4h}^{18} as follows:

$$4\Gamma_{15}+\Gamma_{25}\rightarrow 4[A_{2u}+E_u]+[B_{2u}+E_u] \tag{1}$$

and the symmetries of the modes at R point vary as

$$R'_2+R'_{12}+R_{25}+R'_{25}+2R_{15}\rightarrow A_{2g}+[A_{2g}+B_{1g}]+[A_{1g}+E_g] \\ +[A_{1u}+E_u]+2[B_{2g}+E_g]. \tag{2}$$

Basis functions of irreducible representations for D_{4h} and C_{2v} are listed in Table I and II, respectively. Hereafter, the crystal axes in D_{4h} are denoted by capital letters X, Y and Z and those in C_{2v} are represented by x, y, and z without any suffix. Note that X, Y and Z coincide with edges of a sample with type-I tetragonal domain.[29,30]

Correlations of the symmetry of modes in D_{4h} with those in O_h and C_{2v} are given in Table I. Relations between X, Y, Z in D_{4h} and x, y, z in C_{2v} are not trivial since in the present case C_{2v} is not a simple subgroup of D_{4h}. In Table II, the basis of the irreducible representations of C_{2v} are given in terms of (X,Y,Z) and (x,y,z) separately for the two possible

TABLE II. Irreducible representations for C_{2v}. x,y,z represent the axes in C_{2v}. Relations between x,y,z and X,Y,Z are different for two possible directions of $\vec{P}$. Raman activities in geometry $X(\ ,\ )\bar{Y}$ are given in the last column.

		vector			tensor		Raman activity in $X(\ ,\ )\bar{Y}$
C_{2v}		$\vec{P}\|Y$	$\vec{P}\|X$		$\vec{P}\|Y$	$\vec{P}\|X$	
A_1	z	Y	X	x^2,y^2,z^2	Z^2,X^2,Y^2	Z^2,Y^2,X^2	VV
A_2				xy	ZX	ZY	HV,VH
B_1	x	Z	Z	xz	ZY	ZX	HV,VH
B_2	y	X	Y	yz	XY	YX	HH

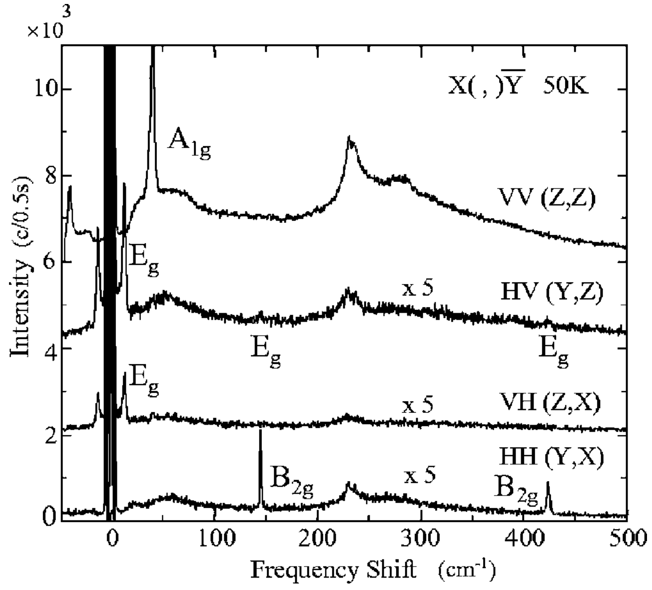

FIG. 3. Polarization dependence of Raman spectra at 50 K from the area A of STO18-96 shown in Fig. 2(a). Scattering geometry is $X(\ ,\ )\bar{Y}$. Spectra satisfy the selection rules for type I tetragonal domain given in Table I.

$\vec{P}$ directions, i.e., $\vec{P} \parallel X$ and $\vec{P} \parallel Y$. In all tables in this paper, the tetragonal domain is assumed to be of type-I and $Z(=[001]_c=[001]_t)$ is taken as x of C_{2v} for both $\vec{P}$ directions. Last column shows that all modes become Raman active in C_{2v}.

B. Raman spectra and the domain types in the tetragonal phase

In order to confirm the type of domains in the tetragonal phase, polarization dependence of Raman spectra from the folded R-point modes were used. From Eq. (2), R_{25} and $2R_{15}$ split into $A_{1g}+E_g$ and $2(B_{2g}+E_g)$, respectively, and they become Raman active below $T_0=108$ K as shown in Table I.

Figure 3 is the spectra at 50 K observed from the area A [in Fig. 2(a)] of STO18-96. A sharp peak at 44 cm^{-1} is seen only in the polarized $VV(Z,Z)$ spectrum, while 15 cm^{-1} peak appears only in the depolarized $HV(Y,Z)$ and $VH(Z,X)$ spectra. As in STO16, the 44 cm^{-1} (it is 45 cm^{-1} in STO16) and 15 cm^{-1} are assigned as A_{1g} and E_g mode from the folded R_{25}. Two sharp but weak peaks at 144, 420 cm^{-1} are observed in the depolarized $HH(Y,X)$ and also very weakly in HV and VH spectra. They are assigned as the folded R_{15} mode (E_g+B_{2g} with almost identical frequencies).

So, all these peaks satisfy the selection rules for D_{4h} given in Table I indicating that the area A is the type I tetragonal domain. If it were the type-II, selection rules are much complicated, for example 44 cm^{-1} A_{1g} mode would be seen in all polarization configurations. Actually, spectra from other parts of this sample did not agree with the selection rules in Table I.

C. Raman spectra in wide frequency range

Polarization and temperature dependencies of Raman spectra from STO18-99 are shown in Figs. 4 and 5 in a wide frequency range up to 800 cm^{-1}. Below 500 cm^{-1}, Fig. 4(a) agrees with those in area A of STO18-96 (Fig. 3). In STO18-97 and -99, whole area were covered by a single type I domain so that the tetragonal axes (X,Y,Z) coincide with the sample edges. In the following sections, we present and discuss on the Raman spectra from these samples.

New peaks appear at 171 and 517 cm^{-1} below T_c as one can see in Figs. 5(a) and 5(b). They are observed in all polarization configurations [Fig. 4(b)].[31–33,3] From IR data in STO16,[7] modes at 171 and 517 cm^{-1} are assigned as TO$_2$ and TO$_4$ of the higher frequency Γ_{15}. IR analysis attributes the 171 cm^{-1} peak also to LO of the lowest Γ_{15} (LO$_1$). It is consistent with our Raman spectra in Fig. 4(b), since from Table II, TO(B_1) mode with displacement parallel to x is active in HV and VH while LO$_1$ is active in VV and HH.[34]

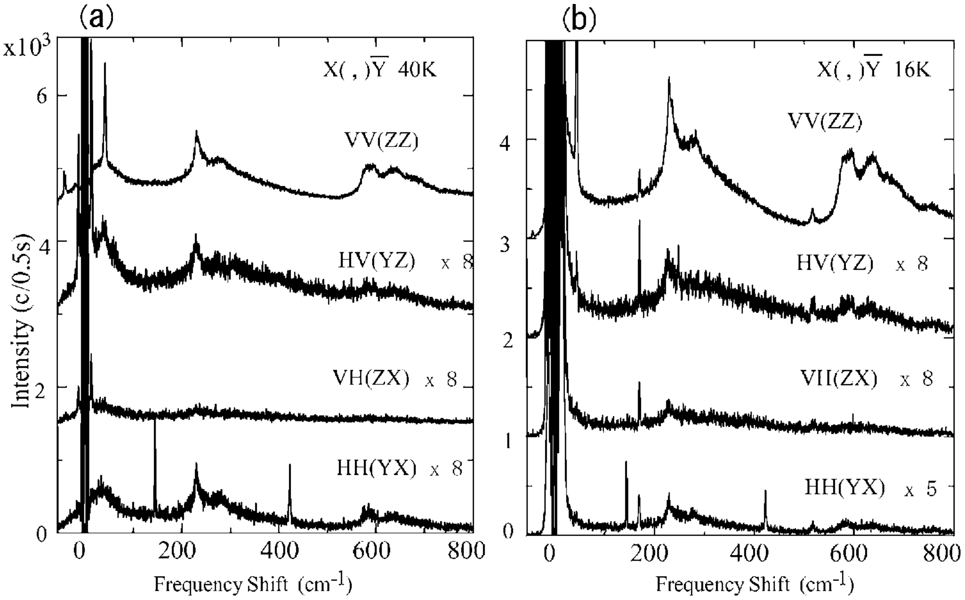

FIG. 4. Polarization dependence of Raman spectra of STO18-99 in a wide frequency range in geometry $X(\ ,\ )\bar{Y}$. (a) at 40 K in the tetragonal phase and (b) at 16 K in the orthorhombic phase. New peaks appear at 171 and 517 cm^{-1} in (b). Mode assignments are given in Table III.

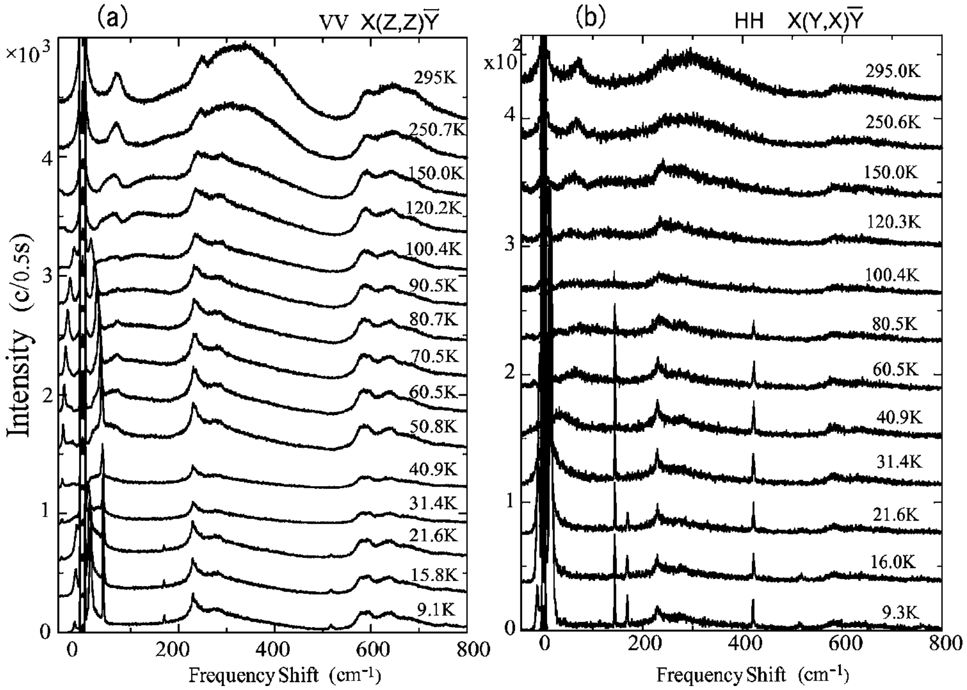

FIG. 5. Temperature dependence of Raman spectra of STO18-99 in a wide frequency range in geometry $X(\ ,\ )\bar{Y}$. (a) polarized spectra $VV(Z,Z)$ and (b) depolarized spectra $HH(Y,X)$. New peaks at 171 and 517 cm^{-1} appear below T_c=24 K in both polarization configurations.

Assignments of the observed modes are given in Table III [for the lower frequency modes in this geometry, see also Table VI(a) in Sec. V E.]

In addition to the sharp peaks, several broad bands are seen near 80, 160, 220, 320, 580, and 640 cm^{-1} [at about 250 K in Fig. 5(a)] in the wide range spectra. Broad bands are due to either the two phonon scattering representing the phonon density of states or the first order scattering caused by local impurities or defects. Some of the broad bands vary with temperature as in Fig. 5. In particular, a weak band at about 160 cm^{-1} (at ~250 K) in STO16 has been assigned as the second order scattering from the lowest $\Gamma_{15}-1$ mode. As one can see in Fig. 5(a), its frequency gradually decrease crossing with another band at 80 cm^{-1} and its broad line shape are distorted on further cooling towards T_0. These behavior in the tetragonal phase are very similar to those reported in STO16.[35–37] Previous studies, however, were done with bulk samples and the domain structures were not taken into account.

V. LOW FREQUENCY PART OF RAMAN SPECTRA

Since all modes related to the ferroelectric soft TO mode from $\Gamma_{15}-1$ and the structural soft mode from R_{25} are ex-

TABLE III. Assignment of the modes observed in the scattering geometry $X(\ ,\ )\bar{Y}$. Detailed assignments of the modes from $\Gamma_{15}-1$ in other geometries are given in Fig. 9. Intensities are shown by symbols: vs (very strong), s (strong), m (medium) and w (weak).

	in D_{4h} (40 K)			in C_{2v} (9 K)		
mode in O_h	freq. (cm^{-1})	intensity	assignment	freq. (cm^{-1})	intensity	assignment
$\Gamma_{15}-1$				17	s in VV, m in HH	q-TO(A_1/B_2)
(ferro. SM)		inactive		17.5	m in HV,VH	TO(B_1)
				171	s in VV, w in HH	q-LO(A_1/B_2)
$\Gamma_{15}-2$		inactive		171	m in VV,HH	q-TO(A_1/B_2)
				171	m in HV,VH	TO(B_1)
$\Gamma_{15}-4$		inactive		517	m in VV,HH	q-TO(A_1/B_2)
				517	m in HV,VH	TO(B_1)
R_{25}	11	s in HV,VH	E_g	11	s in HV,VH	B_1
(struct. SM)				17.5	s in VV	A_2
	44	vs in VV	A_{1g}	44	vs in VV	A_1
R_{15}-1	144	m in HH, w in HV,VH	$B_{2g}+E_g$	144	m in HH, w in HV,VH	$A_2+B_1+B_2$
R_{15}-2	420	m in HH, w in HV,VH	$B_{2g}+E_g$	420	m in HH, w in HV,VH	$A_2+B_1+B_2$

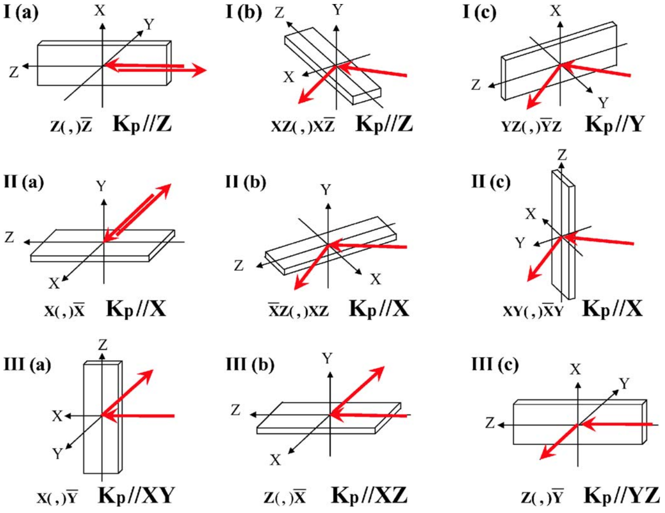

FIG. 6. (Color online) Scattering geometries used in this study. I(a) and I(b) are for phonons with $\vec{K}_p \| Z$ (Raman activities in these geometries are given in Table IV). II(a), II(b), and II(c) are for $\vec{K}_p \| X$ (Table V), III(a) is for $\vec{K}_p \| XY$ (Table VI), and III(c) is for $\vec{K}_p \| YZ$ (Table VII).

pected to be observed below 50 cm^{-1}, low frequency part of the spectra were measured with higher resolution (less than 1 cm^{-1}). Since in strongly polar modes, TO/LO character is dominant over the mode symmetry, it is important to specify the phonon propagation direction $\vec{K}_p=\vec{K}_i-\vec{K}_s$. ($\vec{K}_i$ and $\vec{K}_s$ are wave vectors of the incident and the scattered photon.) Furthermore, for a given $\vec{K}_p$, spectra also depend on the scattering plane determined by $\vec{K}_i$ and $\vec{K}_s$. For these reasons, we measured the spectra in a number of different scattering geometries as illustrated in Fig. 6.[38] For the geometries shown in the third row of Fig. 6, $\vec{K}_p$ is not parallel to any principal axes of crystal below T_c and some modes propagate as an oblique phonon.[39]

A. Raman spectra for $\vec{K}_p \| Z$

First we discuss the case of $\vec{K}_p \| Z$. TO(E_u) mode in D_{4h} is degenerate only in this case.

Table IV shows Raman activities expected in the backward $Z(\ ,\ )\bar{Z}$ and the right angle geometry $XZ(\ ,\ )X\bar{Z}$. Raman tensors are given separately for the two possible directions of $\vec{P}$. TO(E_u) mode in D_{4h} splits into TO(A_1) and TO(B_2) below T_c. In a $\vec{P}\|Y$ domain, the displacement $\vec{u}$ of TO(A_1) is parallel to $Y(=z)$ and that of TO(B_2) is parallel to $X(=y)$. (See also Fig. 9.) Polarization dependence of the spectra measured in the two geometries are given in Figs. 7(a) and 7(b), respectively.

In a backward geometry, scattering plane is not strictly defined. So the polarized spectra *VV* and *HH*, as well as the depolarized spectra *HV* and *VH* in Fig. 7(a) are very similar as they should be. In Fig. 7(a), two rather broad peaks are observed at 12.5 and 20 cm^{-1} and we assigned them as the TO(B_2) and TO(A_1), respectively.

In Table IV, TO(A_1) is active only in *VV* and *HH* and TO(B_2) is active only in *VH* and *HV*. But in Fig. 7(a), both modes are seen in all four polarization configurations. Note, however, that in *VV* and *HH*, TO(A_1) at 20 cm^{-1} is stronger

TABLE IV. Raman activities of TO modes from $\Gamma_{15}-1$ and nonpolar modes from R_{25} in the case of $\vec{K}_p \| Z$. Displacements $\vec{u}$ of TO modes are specified in the first row. Raman tensors α_{ij} (denoted by ij) in the two geometries $Z(\ ,\ )\bar{Z}$ and $XZ(\ ,\ )X\bar{Z}$ [Fig. 6 I(a) and I(b)] are given for each polarization configuration. Polar axis (z) in C_{2v} is assumed to be parallel to either $Y=[110]_c$ or $X=[1\bar{1}0]_c$ and the x axis in C_{2v} is taken parallel to $Z=[001]_c$ for both cases. Corresponding spectra are shown in Figs. 7 and 8. Observed frequencies at about 6 K are given in the bottom row.

			TO($\vec{u}\|Y$) of Γ_{15}		TO($\vec{u}\|X$) of Γ_{15}		Modes from R_{25}					
		in D_{4h}	TO(E_u)				E_g				A_{1g}	
		in C_{2v}	$\vec{P}\|Y$	$\vec{P}\|X$	$\vec{P}\|Y$	$\vec{P}\|X$	$\vec{P}\|Y$		$\vec{P}\|X$		$\vec{P}\|Y$	$\vec{P}\|X$
geometry		polarization	TO(A_1)	TO(B_2)	TO(B_2)	TO(A_1)	A_2+B_1		B_1+A_2		A_1	A_1
$Z(\ ,\ )\bar{Z}$	*VV*	X,X	*yy*	★	★	*zz*	★	★	★	★	*yy*	*zz*
	HV	Y,X	★	*yz*	*zy*	★	★	★	★	★	★	★
	VH	X,Y	★	*zy*	*yz*	★	★	★	★	★	★	★
	HH	Y,Y	*zz*	★	★	*yy*	★	★	★	★	*zz*	*yy*
$XZ(\ ,\ )X\bar{Z}$	*VV*	Y,Y	*zz*	★	★	*yy*	★	★	★	★	*zz*	*yy*
	HV	$X\bar{Z},Y$	★	*zy*	*yz*	★	★	*xz*	★	*xy*	★	★
	VH	Y,XZ	★	*yz*	*zy*	★	★	*zx*	★	*yx*	★	★
	HH	$X\bar{Z},XZ$	*yy*-*xx*	★	★	*zz*-*xx*	★	★	★	★	*yy*-*xx*	*zz*-*xx*
		frequency [cm^{-1}]	20	12.5	12.5	20	17.5		11		44	44
		comment	broad	broad			sharp		sharp		[a]	[a]

[a] 44 cm^{-1} mode is very weak except for *HH* in $XZ(\ ,\ )X\bar{Z}$ which has Raman tensor *xx* (see the text).

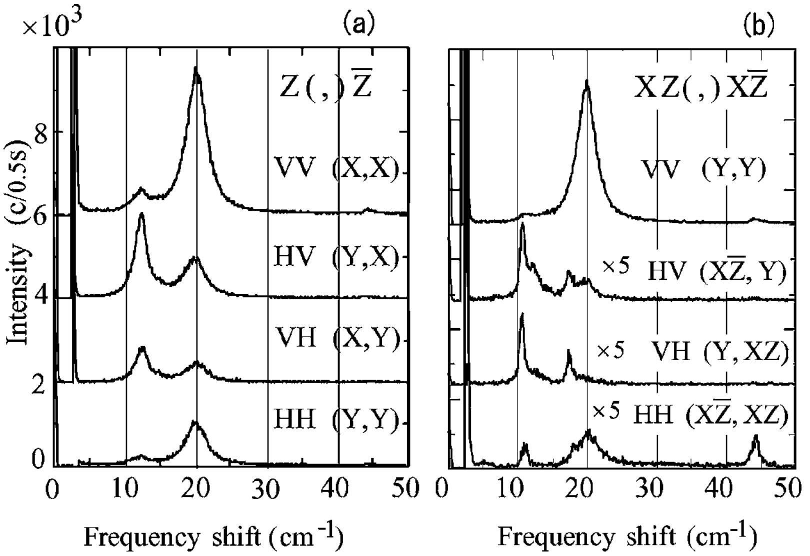

FIG. 7. Polarization dependence of Raman spectra at $T=6$ K for $\vec{K}_p \| Z$ measured in (a) backward geometry $Z(\ ,\ )\bar{Z}$, and (b) right angle geometry $XZ(\ ,\ )X\bar{Z}$.

than TO(B_2) at 12.5 cm^{-1}, and they are in reverse in *VH* and *HV*. So the apparent violation may be intrinsic because these modes are the soft modes (as we shall see later) and the anharmonic coupling between them could be larger than in other modes. Nevertheless, we cannot completely reject the effect of leakage or mixture of polarization. Particularly in the case of $\vec{K}_i \| Z$, the incident laser path is long (7 mm) and its polarization may be partially destroyed during the passage of the sample which includes many ferroelectric domains with $\vec{P} \| X$ and $\| Y$.

In the right angle geometry [Fig. 7(b)], in addition to the broad TO(B_2) at 12.5 cm^{-1}, sharp peaks at 11.0 and 17.5 cm^{-1} are observed in *HV* and *VH*. As expected from Table IV, A_2 and B_1 are Raman active only in this geometry via α_{xy} and α_{xz}. Thus the sharp peaks are assigned as A_2 and B_1 from the E_g mode in D_{4h}. A mode at 20 cm^{-1} weakly seen in *HV* and *VH* is probably the polarization leakage of the strong TO(A_1) mode.

We notice that both of the sharp peaks A_2 and B_1 are observed in the depolarized spectra.[40] If the scattering volume were occupied solely by the area with $\vec{P} \| Y$, only B_1 mode at 17.5 cm^{-1} should be observed, and if it were occupied with $\vec{P} \| X$, only the A_2 mode at 11 cm^{-1} should be observed. This means that the sample is composed equally of domains with $\vec{P} \| Y$ and $\vec{P} \| X$. In other words, the ferroelectric domain size is smaller than the scattering volume, which is

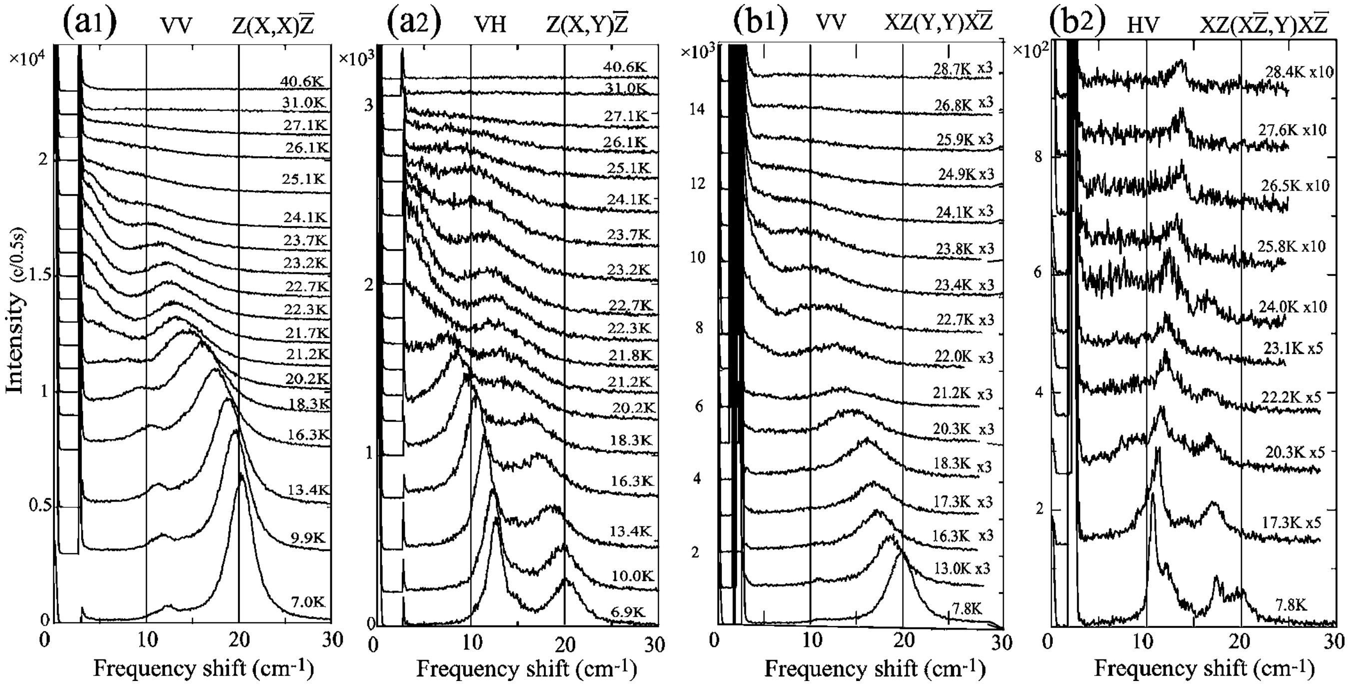

FIG. 8. Temperature dependence of polarized and depolarized spectra for $\vec{K}_p \| Z$. (a1) and (a2) are in the backward geometry $Z(\ ,\ )\bar{Z}$ and (b1) and (b2) are in the right angle geometry $XZ(\ ,\ )X\bar{Z}$. Raman activities and the mode assignment are given in Table IV.

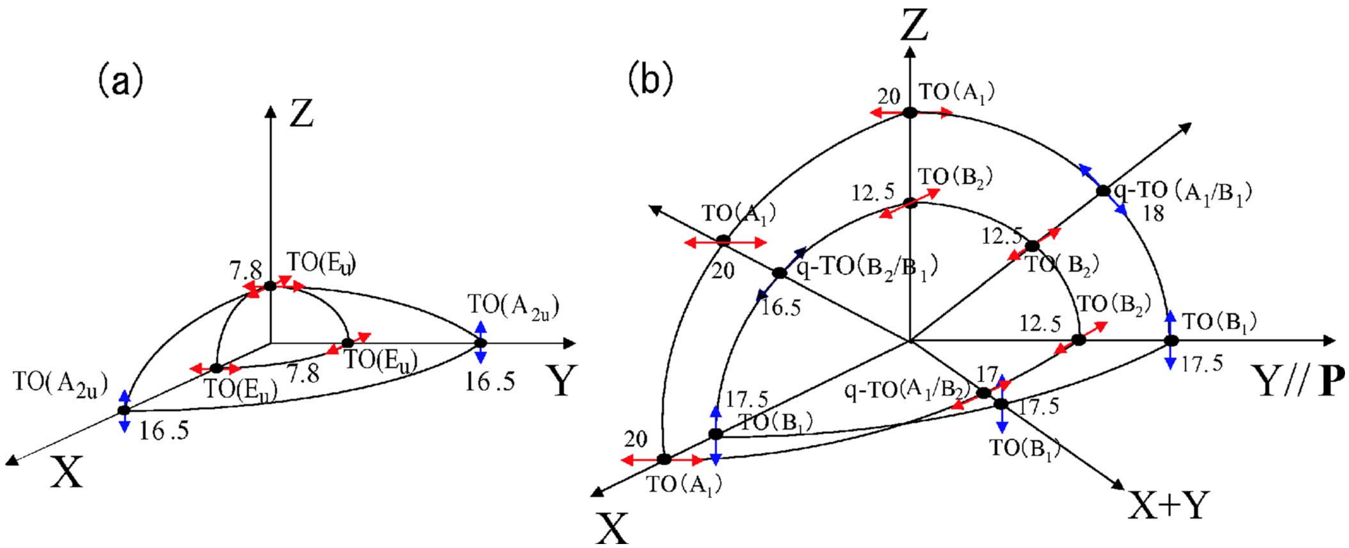

FIG. 9. (Color online) TO-mode frequency surfaces for various directions of phonon propagation vector $\vec{K}_p$. (a) in D_{4h} near T_c. (b) in C_{2v} at $T \ll T_c$. $X=[110]_c$, $Y=[1\bar{1}0]_c$, and $Z=[001]_c$ are the principal axes in the tetragonal phase. (b) is drawn for the case of $\vec{P}\parallel Y$. In case of $\vec{P}\parallel X$, the surface is the mirror image with respect to $X=Y$. Frequencies (in units of cm^{-1}) in (a) are values in STO16 (Ref. 11) and those in (b) are the values at low temperatures measured in the present study. The direction of the displacement for each mode are schematically shown by arrows.

consistent with the optical observation shown in Fig. 2(d).

Figure 7 also suggests that the ferroelectric phase transition has little influence on the structural soft modes from R point. A_1 mode from A_{1g} of D_{4h}, is observed at about 44 cm^{-1} in VV and HH of Fig. 7(b). However, compared with that in Figs. 3 and 4(b), its intensity is extremely weak except for HH of Fig. 7(b). As one can see in Table IV, only for HH of $XZ(\ ,\ )X\bar{Z}$ geometry, Raman tensor α_{xx}, which corresponds to α_{ZZ} in D_{4h}, contributes to this mode. Thus, in contrast to the strong TO(A_1), the weakness of 44 cm^{-1} means that the Raman tensor α_{yy} and α_{zz} for this mode are not enhanced by the transition.

B. Temperature dependence of low frequency modes with $\vec{K}_p \parallel Z$

Figure 8 shows the temperature dependence in the same geometries as Fig. 7. On heating to T_c, softening of TO(A_1) mode at 20 cm^{-1} is seen in VV spectra of both geometries. Softening of the TO(B_2) mode at 12.5 cm^{-1} is clearly seen in VH spectra [Fig. 8(a2)] and very weakly in HV of Fig. 8(b2). Intensities of the soft modes gradually decrease and remain as a broad skirt of the elastic scattering up to a few degrees above T_c.[41]

In Fig. 8(b2), in addition to the soft modes, two sharp peaks are seen as expected from Table IV. The A_2 mode at

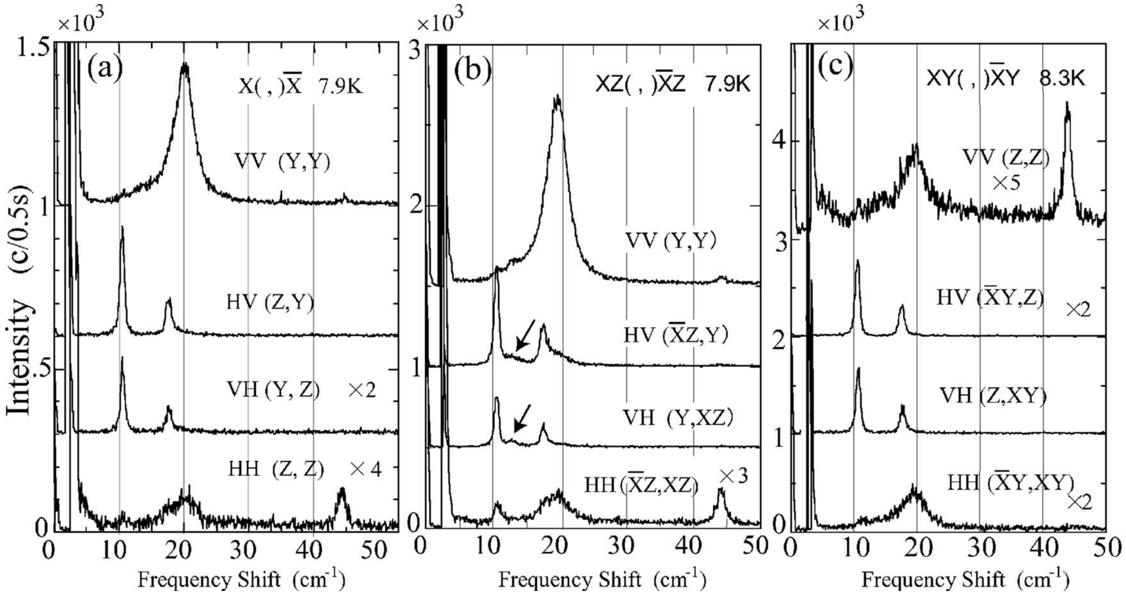

FIG. 10. Polarization dependence of Raman spectra for $\vec{K}_p \parallel X$ measured in three different geometries. (a) backward $X(\ ,\ )\bar{X}$, (b) and (c) right angle $XZ(\ ,\ )\bar{X}Z$ and $XY(\ ,\ )\bar{X}Y$ geometries. Broad shoulder in HV and VH spectra in (b) (shown by arrows) is TO(B_2) mode.

11 cm^{-1} slightly hardens and the weaker B_1 mode at 17.5 cm^{-1} slightly softens on heating and above T_c these modes become E_g at about 14 cm^{-1}.

The most remarkable feature of the spectra with $\vec{K}_p \parallel Z$ is the appearance of strong quasielastic scattering near T_c. It is clearly seen in Figs. 8(a1), 8(a2), and 8(b1) with the width of a few wave number. It becomes stronger on approaching T_c in contrast to the decrease in the soft mode intensities. As shown in later sections, it is observed weakly in the case of $\vec{K}_p \parallel YZ$ (Fig. 14) but almost absent for $\vec{K}_p \parallel X$ (Fig. 11) and for $\vec{K}_p \parallel XY$ (Fig. 13). We shall discuss on the temperature dependence of the soft mode and the possible origin of the quasielastic scattering in Sec. VI.

C. $\vec{K}_p$ dependence of TO modes

Figure 9 illustrates the frequency surfaces of two TO phonons as a function of $\vec{K}_p$. It is based on the results obtained in the present study of Raman spectra with different propagation directions $\vec{K}_p$.

Above and near T_c, TO modes of STO18 are expected to have similar frequencies as STO16. In STO16, TO(E_u) and TO(A_{2u}) at 7 K were observed in hyper-Raman spectra at 7.8 and 16.5 cm^{-1}, respectively.[11] So the TO surfaces in D_{4h} are represented by the ellipsoids with symmetry axis along Z as shown in Fig. 9(a).

Below T_c, the TO surfaces are deformed as shown in Fig. 9(b). It is elongated either X or Y directions, because for temperatures well below T_c, the anisotropy in frequency induced by $\vec{P}$ is expected to be much larger than that of the tetragonality. TO(A_1) frequency in $X-Y$ plane would become much higher than TO(B_2). So in Fig. 9(b), the curve of TO(A_1) in the $X-Z$ plane and that of TO(B_2) in the $Y-Z$ plane would be almost circles but other four curves would be ellipses. In particular, the two ellipses in the $X-Y$ plane will cross at a certain point.

Note that Fig. 9(b) shows the case for $\vec{P} \parallel Y$. In a domain with $\vec{P} \parallel X$, the surface shape is a mirror image of Fig. 9(b) with respect to the vertical plane $X-Y=0$. On approaching T_c, the surfaces in (b) will shrink and they reduce to (a).

D. Raman spectra for $\vec{K}_p \parallel X$

As expected from Fig. 9(b), Raman spectra of phonons with $\vec{K}_p \parallel X$ would be different from those with $\vec{K}_p \parallel Z$. In this case, TO mode symmetries are A_1 and B_1. Since a mode with B_1 symmetry [both B_1 from E_g and TO(B_1) from TO(A_{2u})] has displacement $\vec{u} \parallel Z$, which is perpendicular to $\vec{P}$, it will not be affected by the phase transition. Then its frequency would not be much different from TO(A_{2u}) in STO16 (16.5 cm^{-1}). In other words, the frequency of TO(A_{2u}) mode on X axis in D_{4h} [Fig. 9(a)] and that of TO(B_1) mode on X axis in Fig. 9(b) would be almost the same. In contrast, one

TABLE V. Raman activities of low frequency phonons with $\vec{K}_p \parallel X$ in three different geometries shown in the second row of Fig. 6. Displacements $\vec{u}$ of TO modes are specified in the first row. Corresponding spectra are given in Figs. 10 and 11. Observed frequencies at about 8 K are shown in the bottom row.

			TO($\vec{u} \parallel Y$) from Γ_{15}		TO($\vec{u} \parallel Z$) from Γ_{15}		modes from R_{25}					
		in D_{4h}	TO(E_u)		TO(A_{2u})		E_g				A_{1g}	
		in C_{2v}	$\vec{P} \parallel Y$	$\vec{P} \parallel X$	$\vec{P} \parallel Y$	$\vec{P} \parallel X$	$\vec{P} \parallel Y$		$\vec{P} \parallel X$		$\vec{P} \parallel Y$	$\vec{P} \parallel X$
geometry		polarization	TO(A_1)	TO(B_2)	TO(B_1)	TO(B_1)	A_2+B_1		B_1+A_2		A_1	A_1
$X(\ ,\ )\bar{X}$	VV	Y,Y	zz	★	★	★	★	★	★	★	zz	yy
	HV	Z,Y	★	★	xz	★	★	xz	★	xy	★	★
	VH	Y,Z	★	★	zx	★	★	zx	★	yx	★	★
	HH	Z,Z	xx	★	★	★	★	★	★	★	xx	xx
$XZ(\ ,\ )\bar{X}Z$	VV	Y,Y	zz	★	★	★	★	★	★	★	zz	yy
	HV	$\bar{X}Z,Y$	★	zy	xz	★	★	xz	★	xy	★	★
	VH	Y,XZ	★	yz	zx	★	★	zx	★	yx	★	★
	HH	$\bar{X}Z,XZ$	xx-yy	★	★	★	★	★	★	★	xx-yy	xx-zz
$XY(\ ,\ )\bar{X}Y$	VV	Z,Z	xx	★	★	★	★	★	★	★	xx	xx
	HV	$\bar{X}Y,Z$	★	★	zx	zx	yx	zx	zx	yx	★	★
	VH	Z,XY	★	★	xz	xz	xy	xz	xz	xy	★	★
	HH	$\bar{X}Y,XY$	zz-yy	★	★	★	★	★	★	★	yy-zz	zz-yy
		frequency [cm^{-1}]	20	12.5	17.5	17.5		17.5		11	44	44
		comment	broad	broad		vw		sharp		sharp	[a]	[a]

[a] A_1 mode at 44 cm^{-1} is very weak except for the cases when it has Raman tensor α_{xx}.

of TO(E_u) mode, i.e., TO(A_1) frequency is expected to increase significantly below T_c.

In Table V, expected Raman activities are given for $\vec{K}_p \parallel X$ in three different scattering geometries shown in the second row of Fig. 6. Figure 10 shows the polarization dependence of spectra at about 8 K.

Let us first compare the depolarized spectra, *HV* and *VH* in different geometries. Spectra in the backward geometry with $\vec{K}_p \parallel X$ [Fig. 10(a)] are quite different from the $\vec{K}_p \parallel Z$ case [Fig. 7(a)]. For $\vec{K}_p \parallel Z$, only broad TO(B_2) and TO(A_1) from Γ_{15} were observed. In contrast, in Figs. 10(a) and 10(c), only sharp peaks at 11.0 cm^{-1} (A_2) and 17.5 cm^{-1} [B_1 and TO(B_1)] are observed in agreement with Table V.

The appearance of both A_2 and B_1 modes not only in Fig. 10(c) but also in Figs. 10(a) and 10(b) again supports the coexistence of the small domains with $\vec{P} \parallel X$ and $\vec{P} \parallel Y$ because from Table V, if only $\vec{P} \parallel Y$ domains are in the sample, A_2 mode (via α_{xy}) at 11 cm^{-1} should be observed only in Fig. 10(c).

Table V also predicts that, TO(B_2) is Raman active only in *HV* and *VH* of $XZ(\ ,\ )\bar{X}Z$ geometry. Actually, broad TO(B_2) is observed at 12.5 cm^{-1} in Fig. 10(b) (shown by arrows) and absent in Figs. 10(a) and 10(c).[42]

In the polarized *VV* spectra, strong TO(A_1) mode is seen at 20 cm^{-1} in Fig. 10(a) and 10(b) as expected. The weakness of TO(A_1) (and the relatively strong A_1 mode at 44 cm^{-1}) in Fig. 10(c) is attributed to the same reason as in the case of $\vec{K}_p \parallel Z$, that is, Raman tensor for A_1 symmetry modes is $\alpha_{xx}(\approx \alpha_{ZZ})$ only in this geometry (see Table V). This means again that α_{yy} and α_{zz} are enhanced in the ferroelectric phase while α_{xx} is not enhanced.

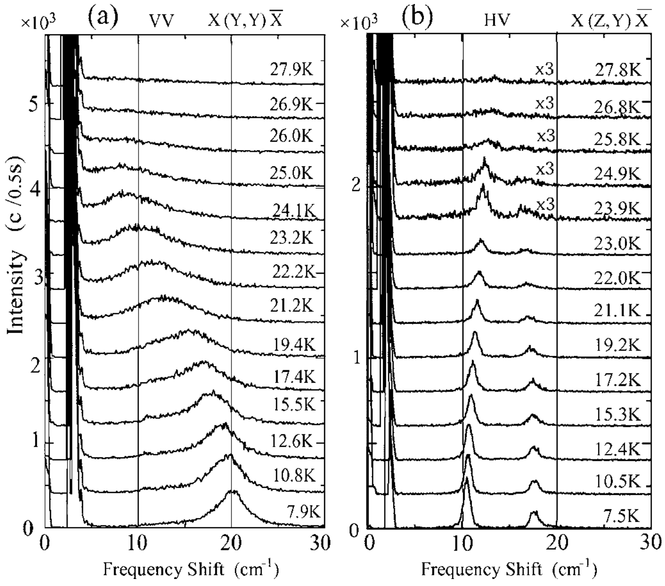

FIG. 11. Temperature dependence of polarized *VV* and depolarized *HV* spectra for $\vec{K}_p \parallel X$ with backward geometry. Softening of TO(A_1) is seen in *VV* spectra.

TABLE VI. Raman activities for low frequency phonons with $\vec{K}_p \parallel XY$ in geometry $X(\ ,\ )\bar{Y}$. $\vec{P}$ is assumed to be parallel to the tetragonal axes X or Y in (a) and parallel to the cubic axes $XY = [100]_c$ or $X\bar{Y} = [1\bar{1}0]_c$ in (b). Displacements $\vec{u}$ of TO modes are specified in the first row. Observed spectra are given in Figs. 12 and 13. Frequencies at about 7 K are given in the bottom row of (a).

			TO($\vec{u} \parallel XY$) from Γ_{15}		TO($\vec{u} \parallel Z$) from Γ_{15}		modes from R_{25}					
	in D_{4h}		TO(E_u)		TO(A_{2u})		E_g				A_{1g}	
(a) C_{2v} with $\vec{P}$ parallel to tetragonal axes												
	in C_{2v}		$\vec{P} \parallel Y$	$\vec{P} \parallel X$	$\vec{P} \parallel Y$	$\vec{P} \parallel X$	$\vec{P} \parallel Y$		$\vec{P} \parallel X$		$\vec{P} \parallel Y$	$\vec{P} \parallel X$
geometry	polarization		q-TO(A_1/B_2)	q-TO(A_1/B_2)	TO(B_1)	TO(B_1)	A_2+B_1		B_1+A_2		A_1	A_1
$X(\ ,\ )\bar{Y}$	*VV*	Z,Z	$xx(A_1)$	$xx(A_1)$	⋆	⋆	⋆	⋆	⋆	⋆	xx	xx
	HV	Y,Z	⋆	⋆	zx	⋆	⋆	zx	⋆	yx	⋆	⋆
	VH	Z,X	⋆	⋆	⋆	xz	xy	⋆	xz	⋆	⋆	⋆
	HH	Y,X	$zy(B_2)$	$yz(B_2)$	⋆	⋆	⋆	⋆	⋆	⋆	⋆	⋆
	frequency [cm^{-1}]		17.0	17.0	17.5	17.5	11	17.5	17.5	11	44	44
(b) C_{2v} with $\vec{P}$ parallel to cubic axes												
	in C_{2v}		$\vec{P} \parallel XY$	$\vec{P} \parallel X\bar{Y}$	$\vec{P} \parallel XY$	$\vec{P} \parallel X\bar{Y}$	$\vec{P} \parallel XY$		$\vec{P} \parallel X\bar{Y}$		$\vec{P} \parallel XY$	$\vec{P} \parallel X\bar{Y}$
geometry	polarization		TO(B_2)	TO(A_1)	TO(B_1)	TO(B_1)	A_2+B_1		B_1+A_2		A_1	A_1
$X(\ ,\ )\bar{Y}$	*VV*	Z,Z	⋆	xx	⋆	⋆	⋆	⋆	⋆	⋆	xx	xx
	HV	Y,Z	⋆	⋆	zx	zx	yx	zx	zx	yx	⋆	⋆
	VH	Z,X	⋆	⋆	xz	xz	xy	xz	xz	xy	⋆	⋆
	HH	Y,X	⋆	yy-zz	⋆	⋆	⋆	⋆	⋆	⋆	yy-zz	yy-zz

Temperature dependence of *VV* and *HV* spectra in geometry $X(\ ,\ )\bar{X}$ are shown in Fig. 11. Softening of TO(A_1) is observed in *VV* [Fig. 11(a)]. It is more clearly seen than in the case of $\vec{K}_p \| Z$ [Fig. 8(a1)] since for $\vec{K}_p \| X$, another TO is TO(B_1) which does not couple with TO(A_1). It is interesting that in contrast to $\vec{K}_p \| Z$, no quasielastic scattering appears near T_c. As we discuss later, it is related to the inactivity of B_2 symmetry mode in this geometry.

Depolarized spectra in the backward geometry with $\vec{K}_p \| X$ [Fig. 11(b)] is also quite different from $\vec{K}_p \| Z$ [Fig. 8(a2)]. As expected from Table V, in the case of $X(\ ,\ )\bar{X}$, TO(B_2) soft mode is not active and only the sharp peaks are observed at 11 and 17.5 cm^{-1}.[43]

All these subtle differences in spectra between $\vec{K}_p \| Z$ and $\vec{K}_p \| X$ and also the differences among the geometries with $\vec{K}_p \| X$ agree excellently with the prediction given in Tables IV and V. Similar set of experiments were performed for $\vec{K}_p \| Y$ and the results are completely the same as those for $\vec{K}_p \| X$.

E. Raman spectra for $\vec{K}_p \| XY$: Remnant of tetragonal structure

$X(\ ,\ )\bar{Y}$ is a simple and interesting geometry since in this case $\vec{K}_p$ is parallel to a cubic axis $[100]_c$. If $\vec{P}$ were along a cubic axis as expected from Slater mode, Raman spectra would be different from the case of $\vec{P}$ parallel to the tetragonal axes. In Table VI, Raman activities in both cases are given separately to clarify the differences. As we shall see below, observed spectra in this geometry are not compatible

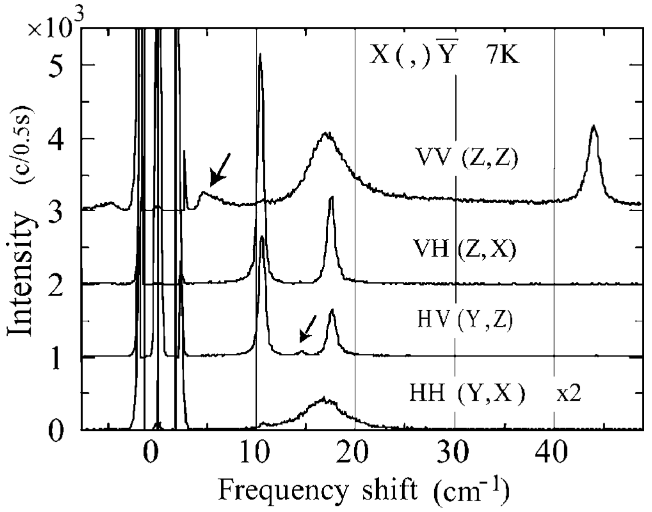

FIG. 12. Polarization dependence in $X(\ ,\ )\bar{Y}$ geometry at 7 K. Note that the frequency of the broad mode observed in *VV* and *HH* is lower than TO(A_1) in Figs. 7 and 10. Peaks shown by the arrows are spurious modes from the remnant tetragonal part of the sample.

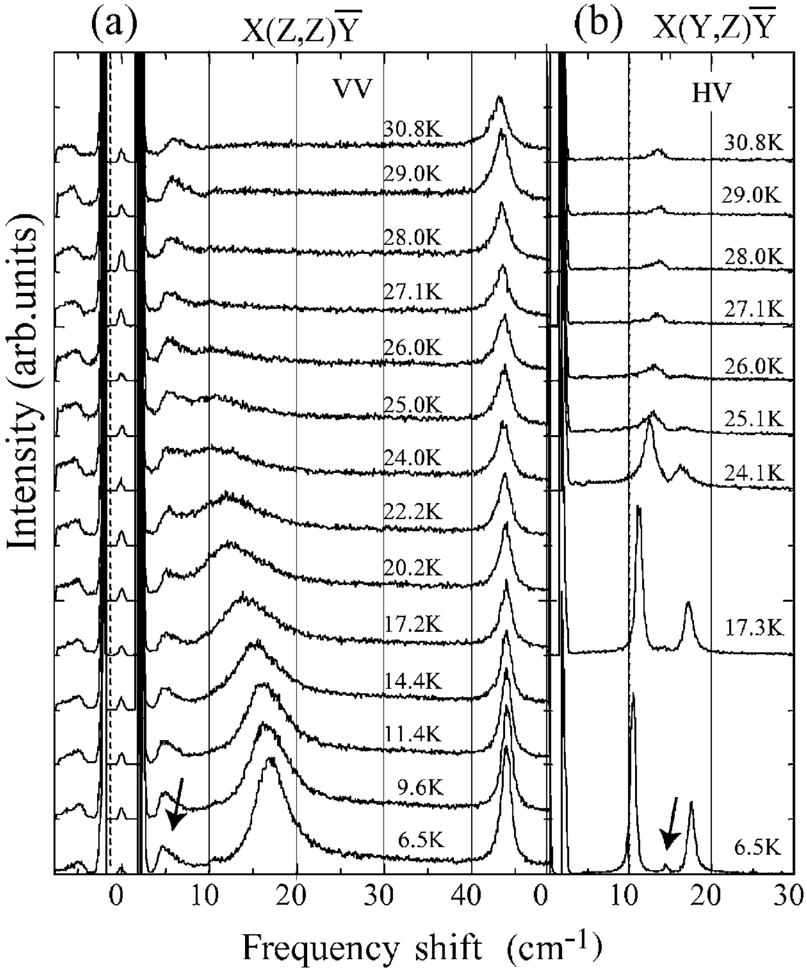

FIG. 13. Temperature dependence of (a) *VV* and (b) *HV* spectra in $X(\ ,\ )\bar{Y}$ geometry. It is qualitatively different from those in Figs. 8 and 11. Spurious modes (shown by arrows) appear at 5 and 14.5 cm^{-1}.

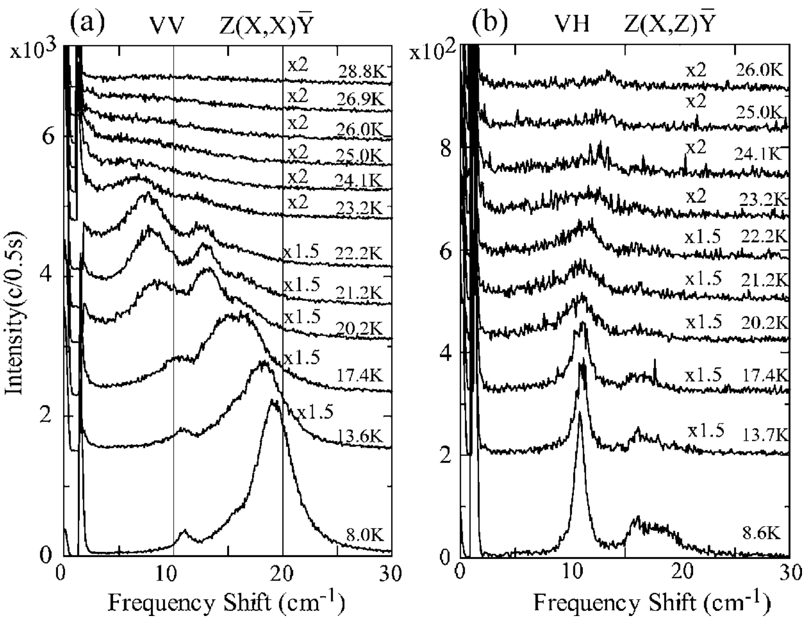

FIG. 14. Temperature dependence of low frequency Raman spectra in $Z(X,Z)\bar{Y}$ geometry. (a) *VV* and (b) *VH*. Note that q-TO(A_1/B_1) in *VV* softens down to about 7 cm^{-1} but does not freeze. Instead, near T_c quasielastic mode appears.

with the assumption of $\vec{P}$ parallel to the cubic axes.

When $\vec{K}_p$ is in the $X-Y$ plane, one of the TO modes [TO(B_1)] is almost independent of the direction of $\vec{K}_p$ and the other TO mode with displacement in the $X-Y$ plane is expected to depend on the angle between $\vec{K}_p$ and $\vec{P}$ since for $\vec{K}_p \| \vec{P}$ it is TO(A_1) and for $\vec{K}_p \perp \vec{P}$ it is TO(B_2). In a general direction of $\vec{K}_p$, it is a quasi-TO(A_1/B_2) mode and its frequency would be between 12.5 and 20 cm^{-1} (see Fig. 9).

Figure 12 is the polarization dependence in $X(\ ,\ )\bar{Y}$ geometry at 7 K, and Fig. 13 is the temperature dependence of *VV* and *HV* spectra. The broad and strong mode in *VV* spectra [Fig. 13(a)] softens on heating as in Fig. 8(a1) ($\vec{K}_p \| Z$) and Fig. 11(a) ($\vec{K}_p \| X$). However, important difference is that its frequency at the lowest temperature is 17 cm^{-1}, which is definitely lower than 20 cm^{-1} of the TO(A_1) mode in Fig. 7 ($\vec{K}_p \| Z$) and Fig. 10 ($\vec{K}_p \| X$).[44] If $\vec{P}$ were parallel to a cubic axis as listed in Table VI(b), the TO mode frequency should be observed at 20 cm^{-1}. So this indicates that the mode observed at 17 cm^{-1} is not pure TO(A_1) but q-TO(A_1/B_2) mode and it strongly supports that $\vec{P}$ is parallel to the tetragonal axes as we assumed.

Unexpected feature of the $X(\ ,\ )\bar{Y}$ spectra not compatible with Table VI(a), is the appearance of the spurious peaks at 5 and 14.5 cm^{-1} (shown by arrows) in *VV* and *HV* (also weakly in *VH*) spectra, respectively. The 5 cm^{-1} peak is almost temperature independent [Fig. 13(a)] and it remains at least up to 40 K with slight hardening on heating above T_c. We note that its line shape is asymmetric with a tail in the higher frequency side. A similar asymmetric line shape has been observed in STO16 at low temperatures and was attributed to a small ferroelectric region in the tetragonal phase.[45] As we shall discuss in the next section, this mode is considered to be the TO(E_u) mode in a remnant part of the tetragonal symmetry in STO18 below T_c. Appearance of a narrow

TABLE VII. Raman activities of phonons with $\vec{K}_p \| YZ$ in geometry $Z(\ ,\ )\bar{Y}$. One of the TO modes in D_{4h} is quasi-TO. Corresponding spectra are shown in Fig. 14. Observed mode frequencies at about 7 K are given in the bottom row.

			TO($\vec{u} \| X$) from Γ_{15}		q-TO($\vec{u} \| \bar{Y}Z$) from Γ_{15}		modes from R_{25}					
	in D_{4h}		TO(E_u)		q-TO(E_u/A_{2u})		E_g				A_{1g}	
	in C_{2v}		$\vec{P} \| Y$ TO(B_2)	$\vec{P} \| X$ TO(A_1)	$\vec{P} \| Y$ q-TO(A_1/B_1)	$\vec{P} \| X$ q-TO(B_2/B_1)	$\vec{P} \| Y$ A_2+B_1		$\vec{P} \| X$ B_1+A_2		$\vec{P} \| Y$ A_1	$\vec{P} \| X$ A_1
geometry	polarization											
$Z(\ ,\ )\bar{Y}$	*VV*	X,X	⋆	*zz*	*yy*(A_1)	⋆	⋆	⋆	⋆	⋆	*yy*	*zz*
	HV	Y,X	*zy*	⋆	⋆	*yz*(B_2)	⋆	⋆	⋆	⋆	⋆	⋆
	VH	X,Z	⋆	⋆	⋆	*zx*(B_1)	*yx*	⋆	*zx*	⋆	⋆	⋆
	HH	Y,Z	⋆	⋆	*zx*(B_1)	⋆	⋆	*zx*	⋆	*yx*	⋆	⋆
	freq.[cm^{-1}]		12.5 broad	20 broad	18 broad	16.5 broad	11.5 sharp	17.5 broad	17.5 broad	11.5 med	44 weak	44 weak

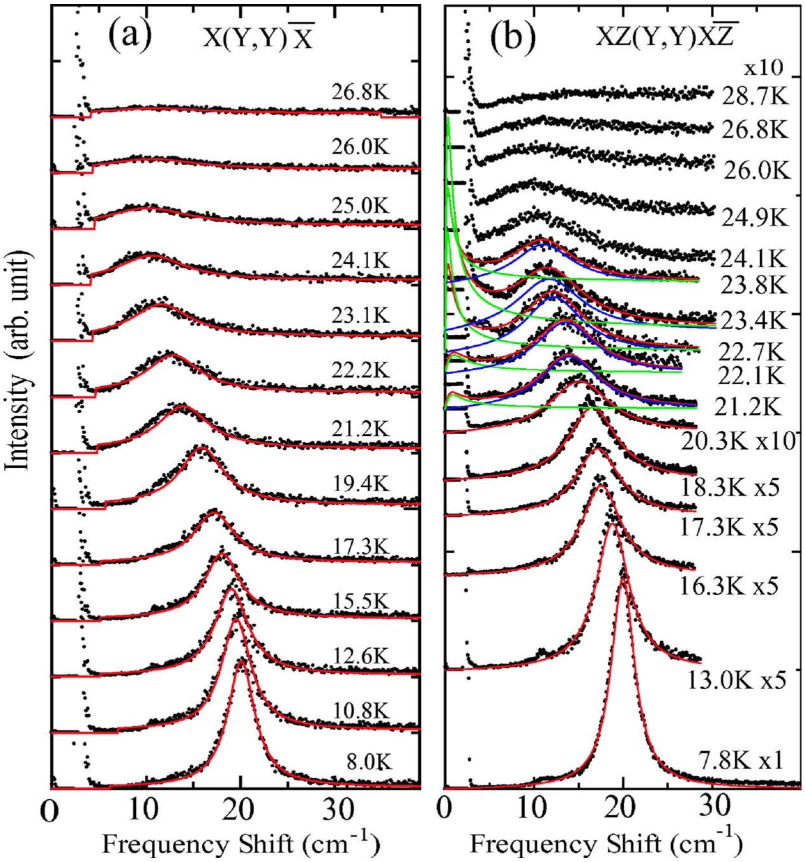

FIG. 15. (Color online) Temperature dependence of the χ spectra and the fitted curves for (a) $X(Y,Y)\bar{X}$ and (b) $XZ(Y,Y)X\bar{Z}$. In (b), curves near T_c are fitted with DHO and Debye formula. Quasielastic scattering near T_c is seen only in (b).

and weak peak at 14.5 cm^{-1} in the depolarized spectra and its temperature independence [Fig. 13(b)] is more evidence for this interpretation.

F. Raman spectra for $\vec{K}_p \| YZ$: Oblique phonons

To complete the $\vec{K}_p$ dependence, Raman spectra for $\vec{K}_p \| YZ$ were investigated. Temperature dependence of *VV* and *VH* are shown in Fig. 14. As shown in Table VII, one of the TO modes in this case has the displacement oblique to *Z*. It is q-TO(E_u) in D_{4h} and becomes q-TO(A_1/B_1) in a $\vec{P}\|Y$ domain and q-TO(B_2/B_1) in a $\vec{P}\|X$ domain. They are observed at 18 and 16.5 cm^{-1}, respectively, in agreement with Table VII (see also Fig. 9). In Fig. 14(a), softening of TO(A_1)+q-TO(A_1/B_1) down to about 7 cm^{-1} is observed. Similar to the case of $\vec{K}_p \| Z$ (Fig. 8), TO(B_2) is seen at 12.5 cm^{-1} via coupling with TO(A_1) and the quasielastic scattering appears and increases on approaching T_c. As we discuss in Sec. VI B, the Raman activity of the B_2 symmetry mode is related to the appearance of the quasielastic scattering.

Temperature dependence of the depolarized VH spectra [Fig. 14(b)] looks similar to Fig. 11(b) for $\vec{K}_p \| X$, but in the $\vec{K}_p \| YZ$ case, the weak softening of q-TO(B_2/B_1) at 16.5 cm^{-1} is overlapped as expected from Table VII.[46]

VI. DISCUSSIONS

Based on the above results which revealed that STO-18 below T_c has C_{2v} symmetry and the spontaneous polarization is parallel to the tetragonal axes, let us discuss several features related to the phase transition at T_c.

A. Temperature dependence of soft mode

Temperature dependence of Stokes side of Raman spectra were analyzed by the formula

$$I(\omega,T) = [n(\omega,T) + 1]\chi''(\omega,T), \qquad (3)$$

where $n(\omega,T)=1/[\exp(\hbar\omega/k_BT)-1]$ is the Bose factor and $\chi''(\omega,T)$ is the imaginary part of the phonon susceptibility. For a damped harmonic oscillator (DHO) with amplitude S, characteristic frequency ω_0 and damping constant γ, $\chi(\omega,T)$ is given by

$$\chi(\omega,T)_{\mathrm{DHO}} = S\frac{\omega_0^2}{\omega_0^2 - \omega^2 - i\omega\gamma}. \qquad (4)$$

The observed data $I(\omega,T)$ divided by $[n(\omega,T)+1]$, which we referred to as χ spectra, were fitted to $\chi''_{\mathrm{DHO}}(\omega,T)$. χ spectra for $X(Y,Y)\bar{X}$ and $XZ(Y,Y)X\bar{Z}$, which correspond to Figs. 11(a) and 8(b1), respectively, are shown in Fig. 15 with the fitted curves. Most data except for those near T_c can be well fitted by DHO function. The main difference between Figs. 15(a) and 15(b) is the appearance of the quasielastic scattering near T_c in (b).

Figure 16 is temperature dependence of the parameters obtained from the analysis. Figure 16(a) shows the frequencies of A_2 and B_1+TO(B_1) modes observed in the geometry $X(Z,Y)\bar{X}$ [Fig. 11(b)]. These modes are almost temperature

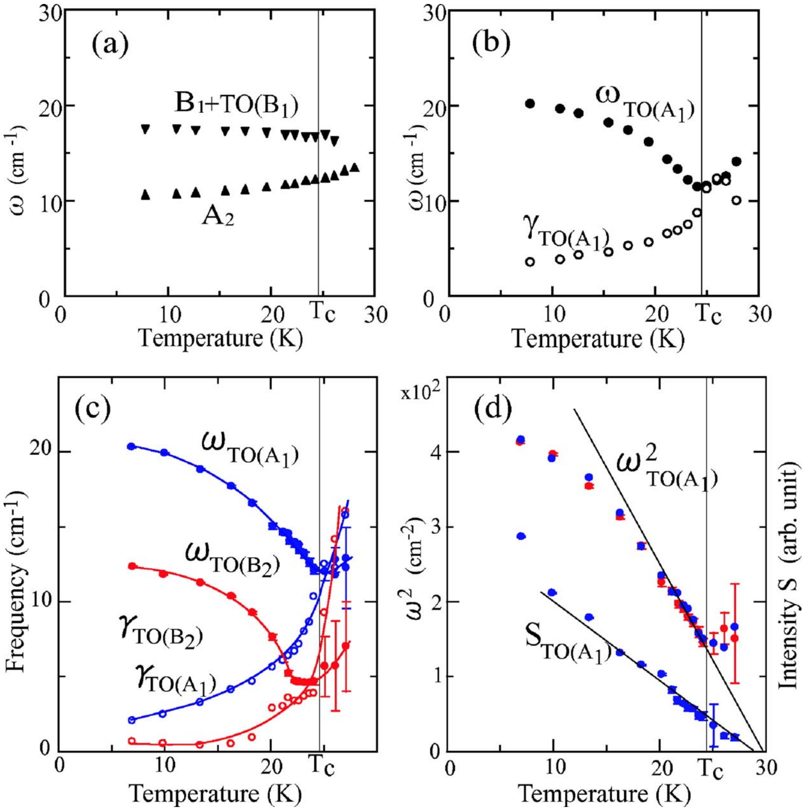

FIG. 16. (Color online) Temperature dependence of the parameters. (a) Frequencies of A_2 and B_1+TO(B_1) observed in $X(Z,Y)\bar{X}$. (b) Frequency and damping constant of TO(A_1) measured in $X(Y,Y)\bar{X}$. (c) Frequency and damping constant of TO(A_1) and TO(B_2) measured in $Z(X,X)\bar{Z}$. (d) Squared frequency of TO(A_1) in (b) and its intensity S.

independent, and above T_c, A_2 and B_1 become the E_g mode at 14.5 cm^{-1} while TO(B_1) remains as TO(A_{2u}) at 17.5 cm^{-1}.

Frequency and damping constant of the soft mode TO(A_1) obtained from the χ spectra [Fig. 15(a)] are shown in Fig. 16(b). In this case ($\vec{K}_p \| X$), only TO(A_1) is observed (Table V). Starting from 20 cm^{-1} at 7 K, the TO(A_1) mode softens on heating. However, the softening ceases at about 10 cm^{-1} and it does not freeze at T_c. The damping constant increases toward T_c but TO(A_1) remains underdamped up to T_c.

Figures 16(c) and 16(d) show the soft mode parameters obtained from the analysis of χ spectra for $\vec{K}_p \| Z$ [Fig. 8(a1), $Z(X,X)\bar{Z}$]. In this geometry, two soft mode TO(A_1) and TO(B_2) are observed. At low temperatures (below ~20 K), they are well fitted to a sum of the independent DHO. TO(B_2) softens from 12.5 cm^{-1} down to about 5 cm^{-1}. Damping constants of these modes also increase towards T_c. Near T_c, however, because of the appearance of the quasielastic component, analysis of the spectra becomes hard. We shall discuss the origin of the quasielastic component in the next subsection.

Figure 16(d) shows the squared frequencies $\omega^2_{\mathrm{TO}(A_1)}$ and its intensity $S_{\mathrm{TO}(A_1)}$. Both of them linearly decrease on heating in the range 15 K$<T<T_c$. They tend to zero toward a temperature $T_c^*=29\pm1$ K, which is several degrees higher than T_c. They are represented by the following equations:

$$\omega_{\mathrm{TO}(A_1)} = 28.0(T_c^* - T)^{1/2}[\mathrm{cm}^{-1}]$$

$$S_{\mathrm{TO}(A_1)} \propto (T_c^* - T). \tag{5}$$

These results show that the TO(A_1) mode follows the conventional Landau theory of soft mode in this temperature range. However, the real transition to the tetragonal phase takes place at T_c before the soft modes might freeze at T_c^*, which is about 5 K higher than T_c.

Despite the existence of the totally symmetric TO(A_1) soft modes, it is important to remember that the eigenvector of TO(A_1), i.e., $\vec{P}$, is parallel to the tetragonal axes. It does not agree with the widely accepted idea that the lowest Γ_{15} mode (so called ferroelectric soft mode) is the Slater mode or some combination of the Slater and Last mode.[6,47] If the freezing of Slater-Last mode takes place, $\vec{P}$ must appear along the cubic axes $[100]_c$ ($X\pm Y$ directions in our notation). This also indicates that the simple soft mode mechanism cannot be the origin of the phase transition in STO18.

The reason why TO(A_1) has higher frequency and stronger than TO(B_2) can be understood by the effect of internal electric field. As well known, a polar phonon produces a macroscopic electric field (the internal field $\vec{E}_{\mathrm{int}}$)[39]

$$\vec{E}_{\mathrm{int}} = -\sqrt{\frac{4\pi M}{V}}\sqrt{\frac{1}{\epsilon_\infty} - \frac{1}{\epsilon_0}}\,\omega_{\mathrm{LO}}\vec{u}, \tag{6}$$

where $\omega_{\mathrm{LO}}=\sqrt{\epsilon_0/\epsilon_\infty}\,\omega_{\mathrm{TO}}$ is the LO mode frequency, M is the effective mass, V is the crystal volume, ϵ_0 and ϵ_∞ are the static and optical dielectric constant, and $\vec{u}$ is the displacement of the polar phonon. This suggests that the soft mode in STO with large TO/LO splitting is sensitive to any kind of electric field. Actually, the effect of an external electric field on the soft mode in STO16 is exceptionally large. It makes the TO(E_u) mode Raman active and shifts its frequency

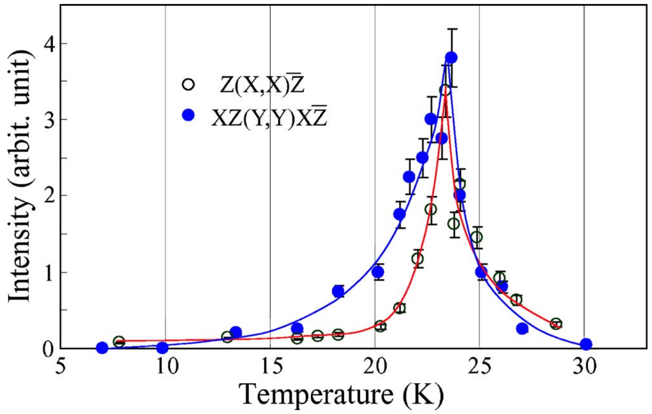

FIG. 17. (Color online) Temperature dependence of the quasielastic scattering intensity observed in $\vec{K}_p \| Z$ spectra. Lines are guides for the eyes.

much higher than that in zero field (from 10 to 44.5 cm^{-1} at 6 K with 12 kV/cm).[48,49] Similar effects of the external field were observed also in STO18.[50]

Then in a ferroelectric domain, macroscopic electric field (depolarization field) $\vec{E}_d = -a\vec{P}$ produced by $\vec{P}$ (a is a positive constant depending on the shape of domains) would also have large influence on the TO mode. The effect is much stronger for TO(A_1) of which displacement is parallel to $\vec{P}$. So the stronger and the higher frequency of TO(A_1) than TO(B_2) is attributed to the effect of the depolarization field.

B. Quasielastic scattering and the orientational ordering of polar cluster

One of the significant features of the observed Raman spectra is the appearance of a quasielastic scattering around T_c. It is most clearly seen in the spectra with $\vec{K}_p \| Z$ (Fig. 8). Adding the Debye formula which represents a relaxational mode with a characteristic time $\tau = 1/\gamma'$,

$$\chi_{\text{Debye}}(\omega) = S_{\text{D}} \frac{\gamma'}{(\gamma' - i\omega)}, \tag{7}$$

χ spectra were analyzed. Some of the fitted curves are shown in Fig. 15(b). Typical value of γ' near T_c was found to be 0.3 cm^{-1} ($\tau \sim 10^{-10}$ s).

Since the spectra below 3 cm^{-1} are masked by the elastic scattering, reliable temperature dependence of τ was hard to obtain but the intensity of the relaxational mode S_D can be estimated by the height of the χ spectra at 4–6 cm^{-1}. Results obtained from $XZ(Y,Y)X\bar{Z}$ and $Z(Y,Y)\bar{Z}$ spectra are shown in Fig. 17. The intensity remarkably increases and takes a maximum near but slightly below T_c. The temperature dependence is similar to that observed in the neutron inelastic scattering.[22]

Although it is not easy to identify the origin of the relaxational mode since quasielastic scattering (or central peak) near T_c may be caused by various slow dynamics related to defects or impurities,[51] we propose below a model which is related to the orientational motion of polarized local clusters in STO.

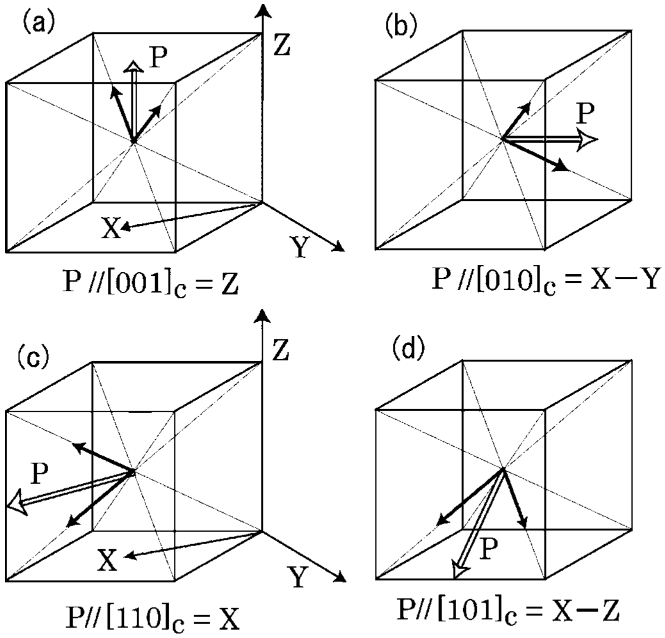

FIG. 18. Possible pair of rhombohedral polar localized clusters (PLC). Net polarization $\vec{P}$ is oriented either in the cubic directions as in (a) and (b) or the tetragonal directions as in (c) and (d). Only the case (c) is compatible with both the ferroelectric interaction and the tetragonal anisotropy.

As mentioned in Sec. I, NMR experiments have revealed that rhombohedral polar clusters exist in the tetragonal matrix both in STO16 and STO18.[23] So the cubic symmetry of the high temperature phase is locally broken in the clusters, and the macroscopic cubic symmetry is the result of time and space averaging. In such a polarized local cluster (let us refer to it as PLC), the Ti ion as well as the Sr ion is displaced to eight possible $[111]_c$ directions. The increase in the intensity and the softening of the TO(E_u) mode in STO18-x (with $x < x_c$) suggests the growth of PLC on cooling in the tetragonal phase.[24]

Taking these results into account, it seems very probable that the appearance of the relaxational mode near T_c and the $\vec{P}$ (parallel to the tetragonal axes) below T_c are closely related to the evolution of PLC.

For high temperatures $T \gg T_c$, the effective dipole moment $\vec{p}$ of a PLC takes randomly one of the eight equivalent $[111]_c$ directions. On cooling, however, as the tetragonal anisotropy increases an isolated $[111]_c$ oriented PLC would become unstable. With the evolution of the PLC, the size and number of PLC would increase and the dipole interactions between a pair of $\vec{p}$ would become gradually strong:

$$\delta U = -J\vec{p}_i \cdot \vec{p}_j \quad (J > 0). \tag{8}$$

Figure 18 shows the possible pairs of $[111]_c$ directed PLCs. In the case of (a), the sum of $\vec{p}$ (denoted as $\vec{P}$) is in $[001]_c = Z$ direction and for the case (b), it is in $[010]_c = X \pm Y$ direction. However, in these cases, the angle between the dipoles is larger than $\pi/2$ and the interactions are antiferroelectric. In contrast, in the case of (c) and (d), the sum $\vec{P}$

is directed to $[110]_c$ and the angle is about 70° giving the ferroelectric interaction. The case (c) would be more stable than (d) since in (c) the sum $\vec{P}$ is in the $X-Y$ plane satisfying the tetragonal anisotropy. Therefore, $\vec{P}$ along the tetragonal axes is realized by the dipole interaction between the $[111]_c+[11\bar{1}]_c$ pair of PLCs.

A pair of PLCs may be regarded as a precursor of a ferroelectric domain. On cooling, it would grow and unite with another pair of PLCs, eventually becoming a ferroelectric domain with macroscopic size. On a heating process, a ferroelectric domain would melt into smaller PLCs or PLC pairs at T_c. During these processes, orientational fluctuations of $\vec{p}$ would increase critically in the vicinity of T_c. If one of the effects of the substitution of ^{16}O by ^{18}O is the increases in the number of PLC and the interaction between PLC, the evolution of the polar clusters will occur easier in STO18 than STO16.

In general, fluctuations of the orientation $\delta\vec{p}_{\perp}$ is much larger than that of the amplitude $\delta\vec{p}_{\parallel}$. Then the symmetry of the orientational fluctuations below T_c would be not A_1 but B_2. This explains why the quasielastic scattering appears strongly only in some geometries.[52] The temperature dependence of Fig. 8(a2) $[Z(X,Y)\bar{Z}]$ clearly shows the situation. Softening of the TO(B_2) mode at 12.5 cm^{-1} is seen up to 20 K. However, on approaching T_c, while the intensity of TO(B_2) decreases, the quasielastic scattering due to the orientational fluctuation with B_2 symmetry ($\perp\vec{P}$) increases significantly. In contrast, in the case of $X(Y,Y)\bar{X}$ [Fig. 11(a)], B_2 is inactive and the quasielastic scattering is absent.[53]

Thus the origin of the quasi-elastic scattering is considered to be the orientational fluctuations of the polarization in the $X-Y$ plane. If this model were the case, the structure of a single PLC would not change at T_c and it explains why the structural variations by this transition are so small and have been hardly observed in STO18.

C. Remnant of tetragonal structure below T_c

Most of the observed Raman spectra satisfy the expected activities for C_{2v}. However, as shown in Fig. 13(a), there appears a spurious peak at 5 cm^{-1} which is not expected from Table VI. This mode is most clearly observed in $X(Z,Z)\bar{Y}$, and we found that it is observed only when its Raman tensor below T_c is α_{xx}, which is the largest component α_{ZZ} in D_{4h}.[54]

Contrary to the soft modes, this mode is temperature independent below T_c and it remains above T_c with gradual hardening on heating [Fig. 13(a)]. The asymmetric line shape of this mode can be understood as the effect of nonspherical shape of a locally polarized region, since a mode with similar line shape was found in STO16 (Ref. 45) and was attributed to the existence of ferroelectric microregion (FMR in their words). All these facts indicate that the 5 cm^{-1} mode is a FMR-like mode in the tetragonal structure which remains below T_c.

As observed optically [Fig. 2(d)], and if the ferroelectric domains are the results of evolution of PLCs as mentioned above, the size of the domains would be small and they would appear in the matrix of the tetragonal structure. Thus, STO18 below T_c does not consist solely of the ferroelectric domains with $\vec{P}\parallel X$ and $\vec{P}\parallel Y$. It contains also remnant of the tetragonal structure as the background of the ferroelectric domains.

VII. SUMMARY AND CONCLUSION

Raman spectra of SrTi^{18}O$_3$ in the ferroelectric phase were studied for various phonon propagation direction $\vec{K}_p$. From the optical measurement and the low frequency Raman spectra from samples with type-I single tetragonal domain, following results were obtained.

(1) In the ferroelectric phase below T_c=24.5 K, granular patterns with a size of 50 μm or smaller were visually observed. From Raman spectra, remnant of tetragonal structure was confirmed below T_c. This indicates that STO18 below T_c is not homogeneous but consists of many ferroelectric domains and the regions with tetragonal structure as the background. This is a quite peculiar nature of STO18 which has not observed in other ferroelectric crystals.

(2) Polarization dependence of the low frequency Raman spectra measured in various scattering geometries were found to satisfy the selection rules for C_{2v} symmetry with the polar axis parallel to either $X=[110]_c$ or $Y=[1\bar{1}0]_c$. This means that the origin of this transition is not the freezing of the Slater mode.

(3) As summarized in Fig. 9, low frequency spectra were well assigned by the TO modes originated from the so-called ferroelectric soft mode (the lowest Γ_{15} in the cubic phase). In case of $\vec{K}_p\parallel Z$, softening of TO(A_1) at 20 cm^{-1} and TO(B_2) at 12.5 cm^{-1} were observed on heating. In case of $\vec{K}_p\parallel X$, only TO(A_1) at 20 cm^{-1} softens. However, the softening of these modes are incomplete and they do *not* freeze at T_c.

(4) Near T_c, critical increase of the quasielastic scattering were observed and a model on its origin is proposed. In this model, the phase transition at T_c is related to the orientational ordering of the rhombohedrally polarized-local-clusters (PLCs), which has been known to exist above T_c.[23] The model explains also why $\vec{P}$ appears parallel to the tetragonal axes.

(5) Sensitive variation in color in the optical observation and the large enhancement of Raman tensors for the soft mode below T_c were observed, indicating that the electronic polarizability varies significantly by the transition. This and the exceptionally large electric field effect on the soft mode[48–50] suggest the variation of the electronic states is involved in this transition.

All these results indicate that, for temperatures far from T_c, the ferroelectric transition in STO18 is triggered by the softening of the TO mode originated from the lowest Γ_{15} mode. However, the fact that polarization $\vec{P}$ is *not* parallel to the cubic axis $[100]_c$ but parallel to the tetragonal axis $[110]_c$ and the nonfreezing of the soft mode at T_c indicate that the origin of the ferroelectricity in STO18 cannot be attributed to the freezing of Slater-Last mode. What happens in the close vicinity of T_c would be the orientational ordering of the polarized local clusters. Therefore, the phase transition in STO-18 is a peculiar transition which has both order-disorder and displacive nature.

An interesting theory which explains the effect of the isotope substitution and the peculiarity of this transition was proposed by Yamada *et al.* using a three state model including the tunneling between the bipolaronic states of TiO_6 clusters[55]. The bilateral nature of displacive and order-disorder in STO18 as well as the role of the electronic polarizability shown in this paper might be related to this model.

Finally we would like to briefly comment on a quite recent paper by Takesada *et al.*[56] They report a perfect softening of the Slater mode in STO18, which is totally different from our results. Their analysis of spectra and the assignment of modes, however, particularly that of A_1 and B_2 below T_c seems quite dubious in view of our analysis. For the correct mode assignment, confirmations of the direction of $\vec{P}$ in C_{2v} symmetry and the $\vec{K}_p$ dependence of spectra would be necessary.

ACKNOWLEDGMENTS

The authors (T.S. and K.A.) thank Keiji Yamashita for his eager collaboration in the early stage of the experiment.

---

[1] K. A. Müller and H. Burkard, Phys. Rev. B **19**, 3593 (1979).

[2] H. Uwe and T. Sakudo, Phys. Rev. B **13**, 271 (1976).

[3] U. Bianchi, W. Kleemann, and J. G. Bednorz, J. Phys.: Condens. Matter **6**, 1229 (1994); U. Bianchi, J. Dec, W. Kleemann, and J. G. Bednorz, Phys. Rev. B **51**, 8737 (1995).

[4] M. Itoh, R. Wang, Y. Inaguma, T. Yamaguchi, Y.-J. Shan, and T. Nakamura, Phys. Rev. Lett. **82**, 3540 (1999).

[5] R. Wang and M. Itoh, Phys. Rev. B **64**, 174104 (2001).

[6] R. A. Cowley, Phys. Rev. **134**, A981 (1964).

[7] A. S. Barker, Jr., Phys. Rev. **145**, 391 (1966).

[8] G. Shirane and Y. Yamada, Phys. Rev. **177**, 858 (1969).

[9] K. Inoue, Ferroelectrics, **52**, 253 (1983); K. Inoue, N. Asai, and T. Sameshima, J. Phys. Soc. Jpn. **50**, 1291 (1981).

[10] H. Vogt, Phys. Rev. B **51**, 8046 (1995).

[11] A. Yamanaka, M. Kataoka, Y. Inaba, K. Inoue, B. Hehlen, and E. Courtens, Europhys. Lett. **50**, 688 (2000).

[12] K. Yamanaka, R. Wang, M. Itoh, and K. Iio, J. Phys. Soc. Jpn. **70**, 3213 (2001).

[13] M. Kasahara, H. Hasebe, R. Wang, M. Itoh, and Y. Yagi, J. Phys. Soc. Jpn. **70**, 648 (2001).

[14] K. Abe, K. Yamashita, Y. Tomita, T. Shigenari, R. Wang, and M. Itoh, Ferroelectrics **272**, 155 (2002).

[15] T. Shigenari, K. Abe, K. Yamashita, T. Takemoto, R. Wang, and M. Itoh, Ferroelectrics **285**, 415 (2003).

[16] M. Yamaguchi, T. Yagi, Y. Tsujimi, H. Hasebe, R. Wang, and M. Itoh, Phys. Rev. B **65**, 172102 (2002).

[17] L. Zhang and W. Kleemann, Appl. Phys. Lett. **81**, 3022 (2002).

[18] Y. Uesu, R. Nakai, N. Kate, C. Minaret, J.-M. Kiat, M. Itoh, M. Narahara, and T. Kyomen, Ferroelectrics **285**, 393 (2003).

[19] H. Hasebe, Y. Tsujimi, R. Wang, M. Itoh, and T. Yagi, Ferroelectrics **272**, 39 (2002).

[20] M. Itoh, R. Wang, M. Narahara, and T. Kyomen, Ferroelectrics **285**, 377 (2003).

[21] T. Ozaki (unpublished).

[22] Y. Noda, K. Mochizuki, H. Kimura, M. Itoh, T. Kyomen, and R. Wang (unpublished).

[23] R. Blinc, B. Zalar, V. V. Laguta, and M. Itoh, Phys. Rev. Lett. **94**, 147601 (2005); B. Zalar, A. Lebar, J. Seliger, R. Blinc, V. V. Laguta, and M. Itoh, Phys. Rev. B **71**, 064107 (2005).

[24] H. Taniguchi, T. Yagi, M. Takesada, and M. Itoh, Phys. Rev. B **72**, 064111 (2005).

[25] W. Kleemann, A. Albertini, M. Kuss, and R. Lindner, Ferroelectrics **203**, 57 (1997).

[26] Relations between T_c and the substitution ratio x is given by $T_c(x)=30.4(x-0.33)^{1/2}$ K (Ref. 5).

[27] K. A. Müller and W. Berlinger, Solid State Commun. **8**, 549 (1970).

[28] T. Akaike, Y. Sakai, T. Shigenari, K. Abe, M. Itoh, and R. Wang (unpublished).

[29] Relations given in Eq. (2) are different from the conventional $R'_{12}\rightarrow A_{2g}+B_{2g}$ and $R_{15}\rightarrow B_{1g}+E_g$ (Ref. 30). The difference is due to the fact that X and Y in D_{4h} of STO is rotated by 45° from cubic axes x_c and y_c. Then basis functions X^2-Y^2 of B_{1g} and XY of B_{2g} in D_{4h} corresponds to $x_c y_c$ of B_{2g} and x_c^2-y_c^2 of B_{1g}, respectively. So we assigned the modes observed in XY configuration in Fig. 3 as B_{2g}.

[30] D. J. Lockwood and B. H. Torrie, J. Phys. C **7**, 2729 (1974).

[31] These peaks, but with slightly different frequencies, were observed in Raman spectra of STO16 with impurities (Ref. 32), as well as Ca-doped (Ref. 3) and thin films (Ref. 33) of STO16, since the local symmetry in those samples is broken by impurity and/or stress.

[32] W. Taylor and A. F. Murray, Solid State Commun. **31**, 937 (1979).

[33] I. A. Akimov, A. A. Sirenko, A. M. Clark, J.-H. Hao, and X. X. Xi, Phys. Rev. Lett. **84**, 4625 (2000).

[34] LO mode displacement in this geometry has both z and y components. Then from Table II it becomes Raman active in VV as A_1 and in HH as B_2, respectively.

[35] D. C. O'Shea and H. Z. Cummins, Solid State Commun. **5**, 241 (1967).

[36] W. G. Nilsen and J. G. Skinner, J. Chem. Phys. **48**, 2240 (1968).

[37] T. Sekine, K. Uchinokura, and E. Matsuura, Solid State Commun. **18**, 569 (1976).

[38] In case of the tilted geometries such as I(b) and I(c) in Fig. 6, the scattering angle inside a sample is less than 90° because of the high refractive index (~2.4) but it is still far from the polariton regime.

[39] R. Loudon, Adv. Phys. **13**, 423 (1964).

[40] Sharp peaks seen weakly in HH may be due to the incomplete cancellation of XZ component (which gives α_{xy} and α_{xz}) in the configuration $(X\bar{Z},XZ)$.

[41] Because of the intrinsic coupling between the soft modes, both TO(A_1) and TO(B_2) are seen in Fig. 8. The apparent difference between the two depolarized spectra [Figs. 8(a2) and (b2)] are probably due to the large scattering volume in the backward geometry $Z(X,Y)\bar{Z}$.

[42] In Fig. 10(b), the weak appearance of TO(A_1) at 20 cm^{-1} in *HV* and A_2 at 17.5 cm^{-1} in *HH* do not agree with Table V. It is probably due to the incomplete cancellation of the *XZ* component in $XZ(\ ,\ )\bar{X}Z$ geometry as in the case of $XZ(\ ,\ )X\bar{Z}$ [Fig. 7(b)].

[43] As in Fig. 8(b2), A_2 (11 cm^{-1}) and B_1 (17.5 cm^{-1}) become E_g at 14 cm^{-1} above T_c. However, in Fig. 11(b), 17.5 cm^{-1} is also assigned as TO(B_1) and it remains (weakly) above T_c as TO(A_{2u}) which is Raman activated in a locally symmetry broken region in D_{4h}.

[44] Note that Fig. 10(c) is very similar to Fig. 12 except for the fact that the mode at 17 cm^{-1} appears at 20 cm^{-1}.

[45] H. Uwe, H. Yamaguchi, and T. Sakudo, Ferroelectrics **96**, 123 (1989).

[46] In this geometry, *HV* spectra (not shown) near T_c is quite different from *VH* [Fig. 14(b)] since TO(B_2) is active only in *HV* as one can see in Table VII.

[47] J. T. Last, Phys. Rev. **105**, 1740 (1957).

[48] P. A. Fleury and J. M. Worlock, Phys. Rev. **174**, 613 (1968).

[49] T. Shigenari and H. Ebashi, J. Phys. C **14**, 969 (1981).

[50] K. Abe, T. Takemoto, O. Sanaka, T. Akaike, T. Shigenari, R. Wang, and M. Itoh, J. Korean Phys. Soc. **46**, 224 (2005).

[51] A. P. Levanyuk and A. S. Sigov, *Defects and Structural Phase Transitions* (Gordon and Breach, New York, 1988).

[52] In $Z(X,X)\bar{Z}$ and $XZ(Y,Y)X\bar{Z}$ [Fig. 8(a1) and 8(b1)] and in $Z(X,X)\bar{Y}$ [Fig. 14(a)], B_2 is active via coupling to A_1 and the quasielastic component is observed.

[53] In $XZ(\ ,\ )\bar{X}Z$ geometry, both B_2 and A_1 are active but, as one can see in Table V, they do not couple since they are active in domains with different $\vec{P}$ directions. So the quasielastic scattering is not observed in *VV* but appears in *VH* and *HV* (spectra not shown).

[54] It appears also weakly in *HH* of Figs. 7(b), 10(a), and 10(b) and *VV* of Fig. 10(c) for which the Raman tensor is α_{xx}. In contrast, in $Z(X,X)\bar{Z}$ [Fig. 7(a)] and $X(Y,Y)\bar{X}$ [Fig. 10(a)], Raman tensors for A_1 mode are not α_{xx} but α_{yy} or α_{zz} and this mode is not observed.

[55] Y. Yamada, N. Todoroki, and S. Miyashita, Phys. Rev. B **69**, 024103 (2004).

[56] M. Takesada, M. Itoh, and T. Yagi, Phys. Rev. Lett. **96**, 227602 (2006).